

Deformation and dewetting of liquid films under gas jets

C. J. OJIAKO^{1,2}, R. CIMPEANU^{3,4,5},
H. BANDULASENA², R. SMITH¹ AND D. TSELUIKO¹

¹ Department of Mathematical Sciences, Loughborough University,
Loughborough, LE11 3TU, UK,

² Department of Chemical Engineering, Loughborough University,
Loughborough, LE11 3TU, UK,

³ Mathematics Institute, Zeeman Building, University of Warwick, Coventry, CV4 7AL, UK,

⁴ Mathematical Institute, Andrew Wiles Building, Radcliffe Observatory Quarter,
Woodstock Road, Oxford, OX2 6GG, UK,

⁵ Department of Mathematics, Imperial College London, London, SW7 2AZ, UK.

(Received ?; revised ?; accepted ?. - To be entered by editorial office)

We study the deformation and dewetting of liquid films under impinging gas jets using experimental, analytical and numerical techniques. We first derive a reduced-order model (a thin-film equation) based on the long-wave assumption and on appropriate decoupling of the gas problem from that for the liquid. To model wettability we include a disjoining pressure. The model not only provides insight into relevant flow regimes, but also is used to guide the more computationally prohibitive direct numerical simulations (DNS) of the full governing equations, performed using two different approaches, the Computational Fluid Dynamics (CFD) package in COMSOL and the volume-of-fluid *Gerris* package. We find surprisingly that the model produces good agreement with DNS even for flow conditions that are well beyond its theoretical range of validity. We find that for thicker films dewetting is dominated by the gas jet and the dry spot heals over time when the gas flow is switched off. For relatively thin films, the gas jet is important for initiating dewetting, which is then dominated by the receding contact line motion, and the dry spot remains dry after the gas flow is switched off. There is also a range of intermediate thicknesses where the gas-induced dewetted spot may remain dry or heal over time, depending on how strong the gas flow that produced the spot was. The observed behaviours are explained using a bifurcation diagram of steady-state solutions in the absence of the gas flow. We additionally compare the computational results with experiments and find good agreement.

Key words:

Introduction

The process of impingement of a gas jet onto a liquid layer is important in numerous industrial applications. For example, it is used in steel production in the basic oxygen furnace process (e.g. Turkdogan 1996; Hwang & Irons 2012), in coating applications in the gas-jet wiping process (e.g. Thornton & Graff 1976; Lacanette *et al.* 2006) and in immersion lithography to remove water from a photoresist coated wafer (e.g. Berendsen *et al.* 2012, 2013). A closely related process is that of impingement of a gas plasma jet (instead of simply a gas jet) onto a layer of a liquid which appears, for example, in the arc

welding process (e.g. Berghmans 1972), in medical applications such as wound healing and skin treatment (e.g. Tian & Kushner 2014; Verlack *et al.* 2018) and in environmental applications such as water treatment and disinfection (e.g. Foster 2017).

The impact of gas jets onto layers of liquids has been previously studied mainly for the case when the layer of the liquid is relatively thick. A gas jet impinging onto a liquid layer exerts normal and tangential stresses on its surface, which result in its deformation creating a cavity and flow inside the liquid. Most of the previous research was focused on analysing the shape of the cavity and its stability. An early experimental study was performed by Banks & Chandrasekhara (1963), who identified three regimes, namely, a steady cavity, an oscillating cavity and splashing. They focused on the analysis of steady cavities and suggested scaling approaches to establish a relation between the impact of the jet and the depth of the cavity. Turkdogan (1966) carried out the Banks & Chandrasekhara (1963) experiments with liquids of different densities but focused on the effects of the gas nozzle diameter and the nozzle distance from liquid surface. Cheslak *et al.* (1969) performed an analysis similar to Banks & Chandrasekhara (1963) and concluded that the occurrence of splashing or a smooth cavity depends on the jet velocity, while the viscosity of the liquid and surface tension are less important. Molloy (1970) studied not only the effect of the gas jet on the cavity, but also the effect of the liquid properties. Previous analytical work investigating the shapes of steady cavities has been mainly based on a conformal mapping approach, in which the flow in the liquid is neglected and the system is assumed to be two dimensional, although both of the assumptions are clearly not valid in practice. The first analytical work using a conformal mapping method was done by Olmstead & Raynor (1964), who studied the cavity shape at relatively small gas velocities in the case of small cavity. Vanden-Broeck (1981) used a similar approach but solved the problem using a different numerical procedure, which allowed analysis of the system for larger gas velocities. A more recent analytical work based on a conformal mapping approach was done by He & Belmonte (2010), who analysed the cavity shape without requiring it to be small. Mordasov *et al.* (2016) employed the balance equations for forces at the gas–liquid interface and not the balance equation for pressure as was used in most previous studies and obtained good agreement with experiments. Despite previous analytical approaches, detailed understanding of the cavity instability mechanisms is still missing. More recent work on gas jets impinging onto liquids has been mainly focused on experimental and DNS investigations (see e.g. Nguyen & Evans 2006; Solórzano-López *et al.* 2011; Liu *et al.* 2015; Muñoz-Esparza *et al.* 2012; Adib *et al.* 2018).

There has been less investigation for the case when the layer of the liquid is relatively thin. In such a case, if the gas jet flow is sufficiently strong, the film ruptures and dewetting is initiated. Gas-jet induced dewetting of thin liquid films was first considered by Berendsen *et al.* (2012, 2013) both experimentally and using modelling, via a reduced-order thin-film equation. In Berendsen *et al.* (2012), the authors focused on analysing the liquid film rupture times and the influence of surfactants and found good agreement between experimental and modelling results. In Berendsen *et al.* (2013), the authors additionally analysed the effect of the movement of the gas jet.

In the present study, we present a comprehensive theoretical and experimental study of the deformation and dewetting of (thin and moderately thin) liquid films in a cylindrical beaker under the influence of an impinging gas jet that is generated by maintaining a constant gas flow rate from a stationary cylindrical tube. To obtain initial insight into relevant flow regimes and timescales of the system, we use a systematically derived thin-film equation that in the axisymmetric case coincides with the model of Berendsen *et al.* (2012). The equation is obtained under the long-wave assumption and by decoupling the

problem for the gas from that for the liquid, under the so-called quasi-static assumption. This involves modelling the gas-liquid interface as a solid wall for the gas problem, which is valid when the typical velocity in the gas is much larger than that in the liquid, see e.g. Tuck (1975) and also more recent work by Tseluiko & Kalliadasis (2011) and Vellingiri *et al.* (2015). Unlike Berendsen *et al.* (2012), we use an iterative procedure for the computation of the normal and tangential stresses exerted by the gas onto the gas-liquid interface which allows us to obtain more accurate results. The thin-film equation is used to guide the more computationally expensive DNS for the full coupled system of the governing equations for our setup, which we perform using two different packages, the CFD package in COMSOL (see e.g. Pryor 2011) with a moving mesh interface and the volume-of-fluid *Gerris* package (see e.g. Popinet 2009). These two packages offer distinct advantages and features improving our understanding of the system. DNS are used to estimate the range of validity of the reduced-order model and allow us, on the one hand, to access regimes that would be inaccessible with the reduced-order model and, on the other hand, to analyse flow characteristics that would be very difficult to image in the experiments reliably (e.g. the velocity field). In addition to studying dewetting, we also analyse the post-dewetting dynamics, when the flow of the gas is switched off. An insight into the expected behaviours for various parameter values is provided by a bifurcation diagram of steady state solutions for the system in the absence of the gas flow.

The manuscript is organised as follows: In § 1 we describe our experimental setup. In § 2 we present the governing equations for the system and derive a reduced order model. Next, § 3 explains our computational framework. In § 4 we present and discuss the results. Finally, in § 5 we give our conclusions.

1. Experimental setup

A schematic representation of the experimental setup is shown in figure 1. We consider a layer of a liquid in a transparent cylindrical beaker and we study the deformation of the surface of the liquid under the influence of an impinging gas jet. The beaker is 6 cm in height and 3 cm in diameter and it is placed in a transparent square tank to minimise the distortion of the image. The liquid used in the experiments is water at room temperature. The gas jet is generated by maintaining a gas flow at a constant rate from a stationary cylindrical tube (nozzle) with its axis coinciding with the axis of the beaker. The inner diameter of the nozzle is 1.6 mm. The nozzle is connected to a compressed gas tank, and the flow rate is controlled by a mass flow controller (MKS, PR4000B). The gas used in most of the experiments is air at room temperature. The nozzle is fixed with a clamp which can be moved to adjust the distance from the nozzle to the surface of the liquid. We typically consider a distance of 5 mm. The position can be read from a movable calibrated scale.

A high-speed camera (Photon Fastcam, M2.1) coupled with a long-distance lens (Infinity, KC) is placed on one side of the square tank in order to record images of the deformed liquid layer. The camera is connected to a computer to enable gathering of the data for analysis. A light source (Kern Dual Fiber Unit LED) is placed on the opposite side of the square tank to provide illumination for the images. The camera is fixed on an adjustable x - y - z stage allowing us to modify the camera's position properly and capture images in the beaker at different places. In particular, the initial position of the camera is adjusted by placing a graticule at the centre of an empty beaker and moving the camera along the stage until the image of the graticule comes into focus. This also allows measuring the size of the interrogation window. An example of an image of the graticule is included in the supplementary material. The recorded images were analysed with the software pack-

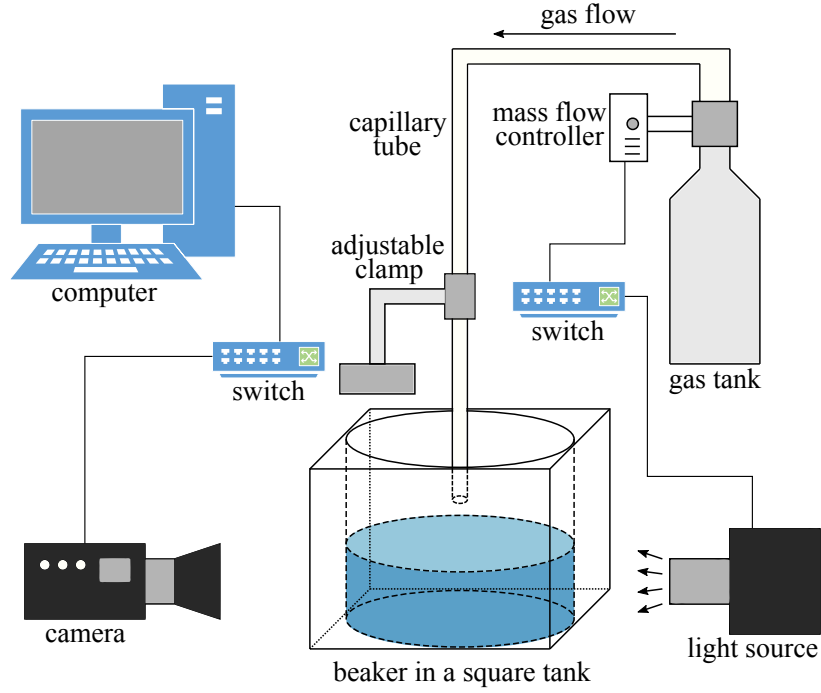


FIGURE 1. Schematic representation of the experimental setup.

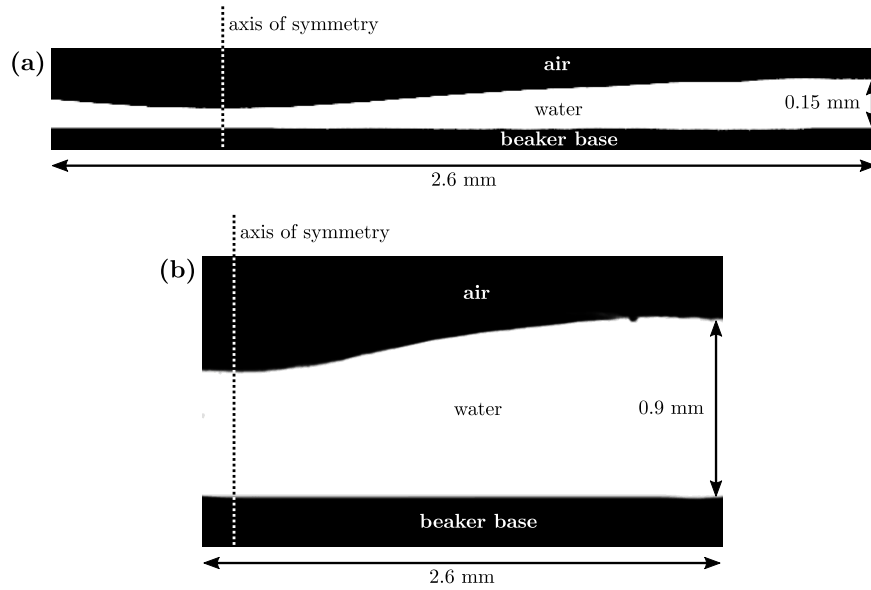


FIGURE 2. Experimental results for (a) an air jet of flow rate 0.15 slpm impinging onto a film of water of thickness 0.2 mm and (b) an air jet of flow rate 0.5 slpm impinging onto a film of water of thickness 1 mm. The images show regions of width 2.6 mm.

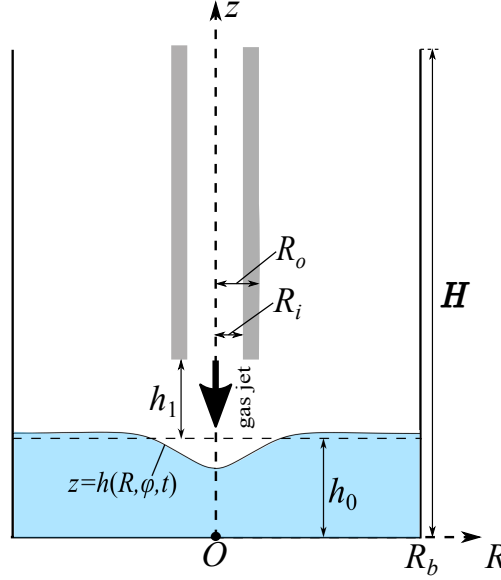


FIGURE 3. Schematic representation of a gas jet impinging onto the surface of a liquid in a cylindrical beaker.

age ImageJ (e.g. Abràmoff *et al.* 2004). Examples of processed recorded images (with increased contrast) are shown in figure 2 for a relatively thin water film (of undisturbed thickness 0.2 mm) in panel (a) and a relatively thick water film (of undisturbed thickness 1 mm) in panel (b). The corresponding raw images are included in the supplementary material. In panels (a) and (b), the water films were deformed by air jets of flow rates 0.15 and 0.5 slpm (standard litres per minute), respectively. The interrogation window for these image was $2.6 \text{ mm} \times 2.6 \text{ mm}$. A deformation of the gas-liquid interface can be clearly seen in both cases. The gas-liquid interface is constructed by curve fitting in the software package Matlab.

2. Mathematical model

2.1. Problem statement and full governing equations

A schematic representation of the model system is shown in figure 3. We denote the radius of the beaker by R_b and its height by H . The thickness of the undisturbed liquid layer is denoted by h_0 . The inner and outer radii of the nozzle are denoted by R_i and R_o , respectively, and the distance between the nozzle and the undisturbed gas-liquid interface is denoted by h_1 . We introduce cylindrical polar coordinates (R, φ, z) with the z -axis pointing upwards along the axis of the beaker in the direction opposite to gravity \mathbf{g} , and with the bottom of the beaker coinciding with the $z = 0$ plane. The deformed gas-liquid interface is denoted by Σ and is given by the equation $f(R, \varphi, z, t) = 0$. In the simplest case, the interface is given by the graph of a function, $z = h(R, \varphi, t)$, and hence $f = h - z$. We assume that the liquid and the gas are of the same constant temperature.

As the gas jet strikes the liquid surface at the centre, the surface of the liquid deforms and a cavity appears. Motion in the liquid, in the form of eddies is also generated. The eddies affect the mass transfer and mixing in the liquid. In order to describe such a system, the Navier-Stokes and continuity equations are used and the corresponding boundary conditions must be satisfied.

As the typical velocity in the liquid will be assumed to be small compared to the speed of sound in the liquid, it is appropriate to model the liquid problem by the incompressible Navier–Stokes equations:

$$\rho_l \frac{D\mathbf{u}}{Dt} = \nabla \cdot \boldsymbol{\sigma}_l + \rho_l \mathbf{g}, \quad \nabla \cdot \mathbf{u} = 0, \quad (2.1)$$

where ρ_l is the liquid density, which is assumed to be constant, \mathbf{u} is the velocity field in the liquid, $D/Dt = \partial/\partial t + \mathbf{u} \cdot \nabla$ is the usual material derivative, and $\boldsymbol{\sigma}_l$ is the viscous stress tensor for the liquid given by

$$\boldsymbol{\sigma}_l = -p_l \boldsymbol{\delta} + 2\mu_l \mathbf{S}_l, \quad (2.2)$$

where p_l is the pressure in the liquid, μ_l is the viscosity of the liquid, which is assumed to be constant, $\boldsymbol{\delta}$ is the identity tensor and $\mathbf{S}_l = \frac{1}{2}[(\nabla \mathbf{u})^T + \nabla \mathbf{u}]$ is the strain-rate tensor.

As we will consider relatively high gas velocities (of up to 50 m/s), compressibility effects may become important in the gas. However, for such gas velocities it is still appropriate to assume that the gas flow is laminar. The Navier–Stokes equation in the gas then takes the form

$$\rho_g \frac{D\mathbf{v}}{Dt} = \nabla \cdot \boldsymbol{\sigma}_g + \rho_g \mathbf{g}, \quad (2.3)$$

where ρ_g is the gas density, \mathbf{v} is the gas velocity and $\boldsymbol{\sigma}_g$ is the viscous stress tensor for the gas given by

$$\boldsymbol{\sigma}_g = -p_g \boldsymbol{\delta} + 2\mu_g \mathbf{S}_g - \frac{2}{3}\mu_g(\nabla \cdot \mathbf{v})\boldsymbol{\delta}, \quad (2.4)$$

where p_g is the gas pressure, μ_g is the viscosity of the gas, which is assumed to be constant, and $\mathbf{S}_g = \frac{1}{2}[(\nabla \mathbf{v})^T + \nabla \mathbf{v}]$ is the strain-rate tensor in the gas.

The continuity equation for the gas is

$$\frac{D\rho_g}{Dt} + \rho_g \nabla \cdot \mathbf{v} = 0. \quad (2.5)$$

In the gas, we need an additional equation of state, and we impose the ideal gas relation $p_g = R_g \rho_g \Theta$, where R_g is the gas constant and Θ is the temperature.

We impose no-slip and no-penetration conditions both for the liquid and for the gas at the solid boundaries ($\mathbf{u} = \mathbf{0}$ and $\mathbf{v} = \mathbf{0}$) except at the beaker side wall, where no-penetration still applies, but instead of no-slip, we impose the Navier slip condition to allow for the motion of the contact line (see, e.g., Sibley *et al.* 2012). So for the liquid when $R = R_b$ we have

$$\mathbf{u} \cdot \hat{\mathbf{t}}_w = \frac{\beta_{NS}^l}{\mu_l} \hat{\mathbf{n}}_w \cdot \boldsymbol{\sigma}_l \cdot \hat{\mathbf{t}}_w, \quad (2.6)$$

where $\hat{\mathbf{n}}_w$ is a unit normal vector to the side wall pointing into the beaker (i.e. $\hat{\mathbf{n}}_w = -\hat{\mathbf{R}}$, where $\hat{\mathbf{R}}$ is a unit vector pointing in the R direction), $\hat{\mathbf{t}}_w$ is a unit tangent vector to the wall, β_{NS}^l is the slip coefficient for the liquid. For the gas when $R = R_b$ we have

$$\mathbf{v} \cdot \hat{\mathbf{t}}_w = \frac{\beta_{NS}^g}{\mu_g} \hat{\mathbf{n}}_w \cdot \boldsymbol{\sigma}_g \cdot \hat{\mathbf{t}}_w, \quad (2.7)$$

where β_{NS}^g is the slip coefficient for the gas.

Note that in (2.6) and (2.7), there are, in general, two independent tangent directions to the wall, i.e. each of the equations results in two scalar equations, by taking $\hat{\mathbf{t}}_w = \hat{\mathbf{k}}$ and $\hat{\mathbf{t}}_w = \hat{\boldsymbol{\varphi}}$, where $\hat{\mathbf{k}}$ and $\hat{\boldsymbol{\varphi}}$ are unit vectors pointing in the z and φ directions. However, we will later assume axisymmetry, i.e. no dependence on φ , and then it will be sufficient to only consider $\hat{\mathbf{t}}_w = \hat{\mathbf{k}}$.

In addition, we impose a fixed contact angle condition at the contact line, so that when the interface is given by $z = h(R, \varphi, t)$, we have

$$\frac{\partial h}{\partial R} = \tan(90^\circ - \theta_c) = \cot \theta_c, \quad (2.8)$$

when $R = R_b$ and $z = h(R_b, \varphi, t)$, where θ_c is the angle the liquid makes with the wall at the contact line.

In a subset of our numerical simulations presented below, at the bottom of the beaker we also impose the Navier slip condition instead of the no-slip condition. This allows us to study dewetting induced by the gas jet using DNS where topological transitions of the gas–liquid interface are allowed. We do this with the volume-of-fluid package *Gerris* (e.g. Popinet 2009), as will be explained below. The contact angle at the bottom of the beaker will be denoted by θ_{eq} . We also performed DNS in the CFD finite-element package COMSOL (e.g. Pryor 2011), and our implementation allows for mesh movements so that the mesh deformations follow the gas–liquid interface motion. Such an implementation allows us to analyse the deformations of the interface very accurately but forbids topological transitions.

At the gas inlet, when $z = h_0 + h_1$ and $0 \leq R \leq R_i$, we impose the fully developed laminar Poiseuille velocity profile:

$$\mathbf{v} = -v_{\max} \left(1 - \frac{R^2}{R_i^2} \right) \hat{\mathbf{k}}, \quad (2.9)$$

where $v_{\max} = 2q_g/\pi R_i^2$, with q_g denoting the imposed gas flow rate.

At the gas outlet, when $z = H$ and $R_o < R < R_b$, we impose normal flow, and prescribe normal stress, i.e. we require $\hat{\mathbf{k}} \cdot \boldsymbol{\sigma}_g \cdot \hat{\mathbf{k}} = -p_a$, where p_a is the atmospheric pressure.

Finally, we discuss conditions that must be satisfied at the gas–liquid interface Σ . First, we have the kinematic condition

$$\frac{Df}{Dt} = 0, \quad (2.10)$$

where we remind that f is a function such that Σ is given by the equation $f(R, \varphi, z, t) = 0$. Continuity of velocity must also be satisfied at the interface, $\mathbf{u} = \mathbf{v}$, and we must have dynamic balance of stress at Σ :

$$\hat{\mathbf{n}} \cdot \boldsymbol{\sigma}_l - \hat{\mathbf{n}} \cdot \boldsymbol{\sigma}_g = \gamma \kappa \hat{\mathbf{n}}. \quad (2.11)$$

Here, $\hat{\mathbf{n}}$ is the unit normal vector to the interface pointing into the liquid. The term on the right-hand side is due to the Laplace pressure, where γ is the gas–liquid surface tension coefficient (which is assumed to be constant) and $\kappa = \nabla \cdot \hat{\mathbf{n}}$ is twice the mean curvature of the interface Σ .

Note that to study dewetting induced by the gas jet in a numerical formulation where topological transitions are not allowed, we also include a Derjaguin (or disjoining) pressure in the stress balance condition. This approach is applicable when Σ is a graph of a function, $z = h(R, \varphi, t)$. The stress balance condition then becomes

$$\hat{\mathbf{n}} \cdot \boldsymbol{\sigma}_l - \hat{\mathbf{n}} \cdot \boldsymbol{\sigma}_g = \gamma \kappa \hat{\mathbf{n}} + \Pi(h) \hat{\mathbf{n}}. \quad (2.12)$$

The disjoining pressure represents an effective interaction between the gas–liquid interface and the liquid–substrate interface. It can be written as $\Pi(h) = -dV(h)/dh$, where $V(h)$ is the so-called binding potential (e.g. de Gennes *et al.* 2013). The disjoining pressure is assumed to be of the form (e.g. Pismen 2002; Galvagno *et al.* 2014)

$$\Pi(h) = -\frac{A}{h^3} + \frac{B}{h^6}, \quad (2.13)$$

where the first term results from the long-range attractive forces (with A representing the Hamaker constant) and the second term results from the short-range repulsive forces. The second term prevents the liquid film from breaking down, and instead of this occurring we obtain a very thin precursor film. In practice, where the film thickness is equal to the thickness of the precursor film, we may assume that a dry spot has appeared. At equilibrium, the thickness of the precursor film corresponds to the minimum of the binding potential $V(h)$ and is equal to $h_{eq} = (B/A)^{1/3}$, with the contact angle at the apparent contact line is given by (e.g. Rauscher & Dietrich 2008; Hughes *et al.* 2015)

$$\theta_{eq} = \cos^{-1} \left(1 + \frac{V(h_{eq})}{\gamma} \right). \quad (2.14)$$

2.2. Thin-film model

Solving the full system of governing equations is a computationally expensive task. We therefore aim to simplify the problem by deriving an accurate reduced-order model. Such a model not only provides insight into the fundamental features of the system in an efficient way but also serves as a mechanism to guide the more computationally prohibitive DNS tools towards suitable regimes with a much more informed view of an otherwise vast parameter space. The first step is to decouple the problem for the gas from that for the liquid, which is possible when the typical velocity in the liquid is much smaller than that in the gas. Then, for the gas problem it is appropriate to neglect the motion of the liquid and to use the quasi-static assumption, i.e. it is appropriate to model the interface as a rigid wall and solve the gas problem independently, see e.g. Tuck (1975) who states that such an assumption is appropriate when the typical liquid velocity is less than approximately 4% of the typical gas velocity, which is always the case in our study (see also Tseluiko & Kalliadasis 2011; Vellingiri *et al.* 2015, for more recent studies, where the quasi-static assumption was used in the modelling of a liquid film sheared by a turbulent gas).

The solution of the gas problem can then be used to obtain the stress exerted by the gas onto the gas–liquid interface, which can then be fed into the normal and tangential stress balance conditions at the interface. We denote such a stress by \mathbf{s}_g so that

$$\mathbf{s}_g = -\mathbf{n} \cdot \boldsymbol{\sigma}_g. \quad (2.15)$$

For the analysis in this section, we first consider the general non-axisymmetric case, and for convenience we use Cartesian coordinates (x, y, z) (so that the z direction remains as before).

We non-dimensionalise the equations using h_0 as the length scale, U_0 as the velocity scale (to be specified later), h_0/U_0 as the time scale and $\mu_l U_0/h_0$ as the scale for pressure and the gas stress, so from now on all the variables will be assumed to be dimensionless. We thus introduce dimensionless variables via the following mappings:

$$(x, y, z, h) \mapsto h_0(x, y, z, h), \quad (u, v, w) \mapsto U_0(u, v, w), \quad (2.16)$$

$$t \mapsto \frac{h_0}{U_0} t, \quad (p_l, \mathbf{s}_g) \mapsto \frac{\mu_l U_0}{h_0} (p_l, \mathbf{s}_g), \quad (2.17)$$

where we denote by u , v and w the x , y and z components of the velocity, respectively.

The incompressible Navier–Stokes and continuity equations in the liquid become

$$Re(u_t + uu_x + vu_y + wu_z) = -p_l x + u_{xx} + u_{yy} + u_{zz}, \quad (2.18)$$

$$Re(v_t + uv_x + vv_y + wv_z) = -p_l y + v_{xx} + v_{yy} + v_{zz}, \quad (2.19)$$

$$Re(w_t + uw_x + vw_y + ww_z) = -p_l z + w_{xx} + w_{yy} + w_{zz} - G, \quad (2.20)$$

$$u_x + v_y + w_z = 0, \quad (2.21)$$

where Re and G are the Reynolds and the gravity numbers, respectively, given by

$$Re = \frac{\rho_l U_0 h_0}{\mu_l}, \quad G = \frac{\rho_l g h_0^2}{\mu_l U_0}. \quad (2.22)$$

The no-slip and no-penetration conditions at the bottom of the beaker become

$$u = 0, \quad v = 0, \quad w = 0 \quad \text{at} \quad z = 0. \quad (2.23)$$

The kinematic condition at the interface, $z = h(x, y, t)$, takes the form

$$w = h_t + uh_x + vh_y. \quad (2.24)$$

The normal stress balance condition takes the form:

$$\begin{aligned} -p_l + \frac{2}{1 + h_x^2 + h_y^2} [h_x^2 u_x + h_y^2 v_y + w_z + h_x h_y (u_y + v_x) - h_x (u_z + w_x) - h_y (v_z + w_y)] \\ = \frac{1}{Ca} \frac{(1 + h_x^2) h_{yy} - 2h_x h_y h_{xy} + (1 + h_y^2) h_{xx}}{(1 + h_x^2 + h_y^2)} - N_s + \bar{\Pi}(h), \end{aligned} \quad (2.25)$$

at $z = h(x, y, t)$, where Ca is the Capillary number given by

$$Ca = \frac{\mu_l U_0}{\gamma}, \quad (2.26)$$

N_s is the dimensionless normal stress exerted by the gas on the gas–liquid interface

$$N_s = \mathbf{s}_g \cdot \hat{\mathbf{n}}, \quad (2.27)$$

which under the quasi-static assumption can be assumed to be a functional of the interface shape, $N_s = N_s[h]$, and finally, $\bar{\Pi}(h)$ is the dimensionless disjoining pressure, given by

$$\bar{\Pi}(h) = -\frac{\bar{A}}{h^3} + \frac{\bar{B}}{h^6}, \quad (2.28)$$

where $\bar{A} = A/\mu_l U_0 h_0^2$ and $\bar{B} = B/\mu_l U_0 h_0^5$.

Taking $\hat{\mathbf{t}} = \hat{\mathbf{t}}_1 = (1, 0, h_x)/\sqrt{1 + h_x^2}$ and $\hat{\mathbf{t}} = \hat{\mathbf{t}}_2 = (0, 1, h_y)/\sqrt{1 + h_y^2}$ in the tangential stress balance condition, we obtain

$$\frac{2h_x(u_x - w_z) + (h_x^2 - 1)(u_z + w_x) + h_y(u_y + v_x) + h_x h_y(v_z + w_y)}{[(1 + h_x^2 + h_y^2)(1 + h_x^2)]^{1/2}} = -T_{s1}, \quad (2.29)$$

$$\frac{2h_y(v_y - w_z) + (h_y^2 - 1)(v_z + w_y) + h_x(u_y + v_x) + h_x h_y(u_z + w_x)}{[(1 + h_x^2 + h_y^2)(1 + h_y^2)]^{1/2}} = -T_{s2} \quad (2.30)$$

at $z = h(x, y, t)$, where T_{si} , $i = 1, 2$, are the $\hat{\mathbf{t}}_1$ and $\hat{\mathbf{t}}_2$ components of the tangential stress exerted by the gas on the gas–liquid interface, $T_{si} = \mathbf{s}_g \cdot \hat{\mathbf{t}}_i$, which under the quasi-static assumption can be assumed to be functionals of the interface shape, $T_{si} = T_{si}[h]$. The tangential stress exerted by the gas on the gas–liquid interface is then expressed as

$$\mathbf{T}_s = T_{s1} \hat{\mathbf{t}}_1 + T_{s2} \hat{\mathbf{t}}_2. \quad (2.31)$$

Next, we utilise the so-called thin-film or long-wave approximation, namely, we assume that the undisturbed film thickness, h_0 , is much smaller than the characteristic horizontal length scale ℓ over which variations in the film thickness occur, and we introduce the so-called thin-film parameter $\epsilon = h_0/\ell \ll 1$. We now use the following additional rescalings of variables that are standard for the thin-film approximation:

$$x = \frac{1}{\epsilon}\xi, \quad y = \frac{1}{\epsilon}\eta, \quad t = \frac{1}{\epsilon}\tau, \quad w = \epsilon W, \quad p_l = \frac{1}{\epsilon}P_l. \quad (2.32)$$

To derive the thin-film equation, we consider the asymptotic limit $\epsilon \rightarrow 0$. Then, to keep capillary effects at leading order, we assume that Ca is asymptotically bounded above and below by ϵ^3 . To neglect inertia at leading order, we assume that $Re \ll 1/\epsilon$. We also assume that $G = O(1/\epsilon)$, so that gravitational effects may enter at leading order. For the disjoining pressure, it is appropriate to assume that $\bar{\Pi} = O(1/\epsilon)$. In addition, for the dimensionless gas stress, we need to assume that $N_s = O(1/\epsilon)$ and $T_{si} = O(1)$, $i = 1, 2$. We then introduce the following rescaled parameters:

$$\tilde{Ca} = \frac{Ca}{\epsilon^3}, \quad \tilde{G} = \epsilon G, \quad (2.33)$$

so that \tilde{Ca} is asymptotically bounded above and below by non-zero constants and $\tilde{G} = O(1)$, and the following rescaled gas normal stress:

$$\tilde{N}_s = \epsilon N_s, \quad (2.34)$$

so that $\tilde{N}_s = O(1)$, and the rescaled disjoining pressure:

$$\tilde{\Pi} = \epsilon \bar{\Pi}, \quad (2.35)$$

so that $\tilde{\Pi} = O(1)$.

The problem at leading order becomes:

$$u_{zz} = P_{l\xi}, \quad v_{zz} = P_{l\eta}, \quad P_{lz} = -\tilde{G}, \quad u_\xi + v_\eta + W_z = 0, \quad (2.36)$$

with the no-slip and no-penetration conditions

$$u = v = W = 0 \quad (2.37)$$

at $z = 0$ and the tangential and normal stress balances

$$u_z = T_{s1}, \quad v_z = T_{s2}, \quad P_l = \tilde{N}_s - \tilde{\Pi}(h) - \frac{1}{\tilde{Ca}}(h_{\xi\xi} + h_{\eta\eta}) \quad (2.38)$$

at $z = h(\xi, \eta, \tau)$. We also have the kinematic condition, which can be rewritten as

$$h_\tau + \nabla \cdot \mathbf{q} = 0, \quad (2.39)$$

where $\nabla = (\partial/\partial\xi, \partial/\partial\eta)$ and

$$\mathbf{q} = \left(\int_0^h u \, dz, \int_0^h v \, dz \right) \quad (2.40)$$

is the flux vector parallel to the plane $z = 0$.

Then we find that the pressure at leading order is given by

$$P_l = -\tilde{G}(z - h) + \tilde{N}_s - \tilde{\Pi}(h) - \frac{1}{\tilde{Ca}}\nabla^2 h, \quad (2.41)$$

and the velocity components at leading order are given by

$$(u, v) = \left(\frac{z^2}{2} - hz \right) \nabla P_l + z \mathbf{T}_s, \quad (2.42)$$

$$w = - \left(\frac{z^3}{6} - \frac{z^2 h}{2} \right) \nabla^2 P_l + \frac{z^2}{2} \nabla P_l \cdot \nabla h - \frac{z^2}{2} \nabla \cdot \mathbf{T}_s. \quad (2.43)$$

Substituting the leading-order expressions for u and v into the expression for the flux vector (2.40), we find that at leading order

$$\mathbf{q} = -\frac{h^3}{3} \nabla P_l + \frac{h^2}{2} \mathbf{T}_s. \quad (2.44)$$

Substituting this expression into the kinematic condition (2.39) gives the following evolution equation for the film thickness, the so-called thin-film equation:

$$h_\tau + \nabla \cdot \left(-\frac{h^3}{3} \nabla P_l + \frac{h^2}{2} \mathbf{T}_s \right) = 0. \quad (2.45)$$

Scaling back to the dimensionless variables x , y and t , we obtain

$$h_t + \nabla \cdot \left(-\frac{h^3}{3} \nabla p_l + \frac{h^2}{2} \mathbf{T}_s \right) = 0, \quad (2.46)$$

where the dimensionless leading-order pressure is given by

$$p_l = -G(z - h) + N_s - \bar{\Pi}(h) - \frac{1}{Ca} \nabla^2 h \quad (2.47)$$

and $\nabla = (\partial/\partial x, \partial/\partial y)$.

For convenience, it is possible to eliminate one of the dimensionless parameters by, for example, multiplying the thin-film equation by Ca and appropriately rescaling time. This is equivalent to choosing $U_0 = \gamma/\mu_l$, for which the time scale becomes $\mu_l h_0/\gamma$ and the scale for pressure and the gas stress becomes γ/h_0 . Then the pressure in the thin-film equation takes the form

$$p_l = -Bo(z - h) + N_s - \bar{\Pi}(h) - \nabla^2 h, \quad (2.48)$$

where Bo is the Bond number given by

$$Bo = G Ca = \frac{\rho_l g h_0^2}{\gamma}, \quad (2.49)$$

and the dimensionless coefficients in the disjoining pressure are $\bar{A} = A/\gamma h_0^2$ and $\bar{B} = B/\gamma h_0^5$.

For the validity of the thin-film equation in terms of dimensionless parameters that are independent of U_0 , we must have $Bo = O(\epsilon^2)$ and $La \ll 1/\epsilon^4$, where La is the Laplace number given by

$$La = \frac{Re}{Ca} = \frac{\gamma \rho_l h_0}{\mu_l^2}. \quad (2.50)$$

The latter condition is needed for inertia to be negligible. We must additionally have $N_s = O(\epsilon^2)$ and $T_{si} = O(\epsilon^3)$, $i = 1, 2$. The validity of the thin-film equation for the experimental parameter values that we have used is discussed § 4.

Finally, going back to cylindrical polar coordinates (R, φ, z) and assuming axisymmetry, we obtain the following equation:

$$h_t + \frac{1}{R} \left[-\frac{Rh^3}{3} p_{lR} + \frac{Rh^2}{2} T_s \right]_R = 0, \quad (2.51)$$

where T_s denotes the gas tangential stress in the R -direction and pressure is given by

$$p_l = -Bo(z - h) + N_s - \bar{\Pi}(h) - \frac{1}{R}(Rh_R)_R. \quad (2.52)$$

Note that here R is assumed to be non-dimensionalised using h_0 as the length scale. To solve the thin-film equation (2.51) numerically, we also need to impose appropriate boundary conditions. Conditions at $R = 0$ follow from the symmetry assumption:

$$h_R = h_{RRR} = 0 \quad \text{at} \quad R = 0. \quad (2.53)$$

At the side wall, we will assume for simplicity that the contact angle is 90° , so that

$$h_R = 0 \quad \text{at} \quad R = \bar{R}_b, \quad (2.54)$$

where $\bar{R}_b = R_b/h_0$, and we will impose zero flux in the R direction, so that

$$q \equiv -\frac{h^3}{3}p_{lR} + \frac{h^2}{2}T_s = 0 \quad \text{at} \quad R = \bar{R}_b. \quad (2.55)$$

For analysing flow patterns in the liquid film, it is also useful to give the R and z velocity components in cylindrical polar coordinates:

$$u^R = p_{lR} \left(\frac{z^2}{2} - hz \right) + T_s z, \quad (2.56)$$

$$w = -\frac{1}{R}(Rp_{lR})_R \left(\frac{z^3}{6} - \frac{h}{2}z^2 \right) + \frac{p_{lR} h_R z^2}{2} - \frac{1}{2R}(RT_s)_R z^2. \quad (2.57)$$

3. Computational framework

Complementing the experimental and analytical investigations we also considered two distinct numerical platforms to simulate the target physical system. The two packages (described in more detail in the paragraphs to follow) offer distinct advantages and features that aid our understanding of the flow characteristics. They act not only to bridge the gap between the previous approaches, but also to access regimes that would be inaccessible with a reduced-order model approach on the one hand, as well as easily allow the inspection of quantities in the flow that would be very difficult to image reliably on the other.

First, we implemented the setup in the commercial software platform COMSOL Multiphysics 5.3a. We used the CFD module which is a standard tool to simulating systems that involve complex fluid flow models. A two-dimensional axisymmetric geometry was built using the parameters from the experiments. COMSOL uses an unstructured mesh finite-element approach, which is highly suitable for tracking details near specific target regions of the domain. However, for the present problem, we found it challenging and computationally highly expensive to accurately describe the evolution of the gas-liquid interface and topological transitions, occurring e.g. in the dewetting process, using the built-in level-set and phase-field methods. We thus utilised a more computationally efficient moving-mesh approach in which the gas-liquid interface is modelled as a sharp surface separating the two phases and the mesh deformations follow the deformations of the interface. However, such an implementation is not directly suitable for describing topological transitions such as in the dewetting process. Thus, as discussed in § 2.1, we included the disjoining pressure into the normal stress balance condition to study dewetting which prevents the liquid film from breaking down so that a dry spot is modelled with a very thin precursor film. We should note that this approach still has limitations

in modelling dewetting. For example, it is not suitable for describing dewetting on hydrophobic surfaces for which the contact angle is greater than 90° .

To overcome the limitations of our COMSOL implementation with respect to topological transitions, we also implemented the setup in the open-source package *Gerris* (e.g. Popinet 2009). Well-known in the interfacial flow community for more than a decade, its strengths lie in the adaptive mesh refinement and parallelisation capabilities that make it an ideal testbed for multi-scale flow problems. The transparent structure of the code allows for careful validation of any in-house implemented extensions, as have been employed here. For example, one particular region of interest in the flow is the near-wall region where dewetting can be considered without the need to introduce a precursor film. The interface-capturing techniques, coupled with well-established contact line models (e.g. Afkhami *et al.* 2018) and control over any imposed Navier-slip-type conditions, provide an added perspective to the overall investigation. The chosen refinement strategy concentrates on adequately addressing the sensitive regions near the gas nozzle and the walls in contact with the liquid, while adaptive refinement is used to steer degrees of freedom towards any changes in interfacial position, as well as changes in components of the velocity field and vorticity in order to accurately capture non-trivial flow regions in both the liquid and the gas.

The runs in the sections to follow have been executed in parallel on local computing facilities, typically amounting to $O(10^3)$ CPU hours in *Gerris*, depending on flow parameters. While the chosen adaptive strategy restricts the number of gridnodes to $O(10^5)$, a gain of two orders of magnitude over a uniform grid with the same minimum cell size, the delicate interplay between the gas-liquid coupling requires special measures from a linear algebra and stability viewpoint, leading to relatively small time steps in exchange for mesh-independent results. By contrast, we found that the computations in COMSOL were significantly faster for a similar number of degrees of freedom (we typically used $O(10^5)$ triangular elements), with a typical computation for the fully coupled problem taking approximately $O(10^2)$ CPU hours. However, as already noted above our implementation in COMSOL has its restrictions for systematically studying dewetting.

We have validated both implementations extensively by systematically decreasing the cell size or increasing the number of mesh elements until the convergence in the numerical results was achieved. The results of the computations and comparisons with the experimental and reduced-order model results are presented in the next section.

4. Results

Throughout this section, we consider the following geometrical parameters in both the mathematical model and in the numerical simulations: the diameter of the beaker is 3 cm and its height is 6 cm; the inner diameter of the gas nozzle is 1.6 mm and its distance from the undisturbed liquid surface is 5 mm, as in the experiments. Also, the liquid is water and the gas is air at room temperature. The density and viscosity of water at room temperature are $\rho_l = 1000 \text{ kg m}^{-3}$ and $\mu_l = 8.9 \times 10^{-4} \text{ Pa s}$, respectively. For the density and viscosity of air, we use $\rho_g = 1.22 \text{ kg m}^{-3}$ and $\mu_g = 1.81 \times 10^{-5} \text{ Pa s}$. The surface tension coefficient for the air-water interface is set to $\gamma = 72 \times 10^{-3} \text{ N m}^{-1}$. Regarding the results obtained with the thin-film equation (2.51), for the asymptotic validity of the equation $Bo \ll 1$ is required and also $La \ll 1/Bo^2$. It can be verified that for a water film La becomes smaller than $1/Bo^2$ if $h_0 < 0.226 \text{ mm}$ (and then $Bo < 0.007$). Thus, strictly speaking for the validity of the thin-film model the thickness of the film must be less than $\approx 0.23 \text{ mm}$. As regards gas flow rates suitable for the validity of the thin-film equation, we note that for a film of thickness 0.226 mm and an air jet flowing at the rate

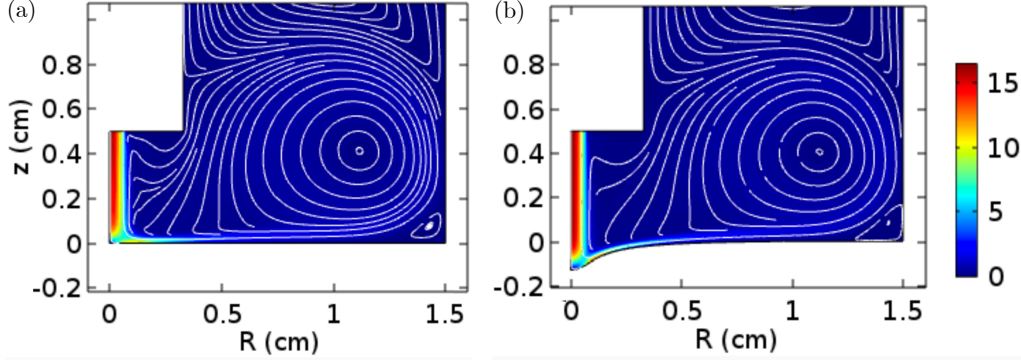


FIGURE 4. Numerical solutions at steady state of the decoupled gas problem for the gas flow rate $q_g = 1$ slpm obtained using COMSOL. The colour scheme illustrates the gas speed in metres per second as indicated in the colourbars and the white thin lines show streamlines. (a) Gas jet impinging onto the interface modelled as a flat wall. (b) Gas jet impinging onto the interface modelled as a deformed wall, with the shape of the deformation obtained by solving the problem for the liquid film using the thin-film equation (2.51) with the gas stresses obtained from the solution shown in panel (a), when the interface is modelled as a flat wall.

0.2 slpm, the maximum values of the normal and tangential stresses non-dimensionalised with γ/h_0 turn out to be 0.007 and 0.0008, respectively, which is appropriate for the validity of the model. For an air jet flowing at the rate 0.4 slpm, the maximum values of the dimensionless normal and tangential stresses turn out to be 0.028 and 0.0025, respectively, which is also close to the region of the validity of the model. However, it will be shown below that the thin-film equation turns out to produce good agreement with DNS and experiments also for film thicknesses significantly larger than 0.226 mm (of $O(1)$ mm) and for gas flow rates significantly higher than 0.4 slpm (of $O(1)$ slpm). For even thicker water films and higher gas flow rates, inertial effects become important and the derived thin-film equation is not valid. Such parameter regimes can be accessed with the developed DNS framework.

4.1. Decoupled gas problem

First, we discuss the decoupled gas problem and explain how the gas normal and tangential stresses exerted on the interface are computed using an iterative procedure. Under the quasi-static assumption, we model the liquid surface as a solid wall obtaining a problem for the gas only, and initially we assume that the interface is flat. The gas flow rapidly develops into a steady state. The resulting gas flow pattern at steady state obtained using COMSOL is shown in figure 4(a) for the gas flow rate $q_g = 1$ slpm, which corresponds to the maximum gas speed of approximately 16 m s^{-1} . In this section, we assume that the undisturbed interface is located at $z = 0$. We note that *Gerris* simulations agree with the COMSOL results. The colour scheme indicates the gas speed in metres per second and the thin white lines show streamlines. We can observe that the gas jet impinges onto the lower wall, and then the gas flows in the direction parallel to the wall radially outwards with its speed decreasing as the radial distance increases. We can also observe that a relatively large recirculation zone (eddy) is generated in the gas, and there is also a small, relatively slow eddy in the bottom-right corner. This solution of the gas problem for the interface modelled as a flat solid wall is used to compute the normal and tangential stresses exerted by the gas jet on the interface at different radial locations. Next, we use these stresses in the thin-film equation (2.51) to solve the problem for the liquid film and therefore obtain the deformation of the interface resulting from these stresses. The

thin-film equation is solved numerically in Matlab using finite-difference approximations for the spatial derivatives and Matlab's *ode15s* solver for stepping in time. For this gas flow rate, the solution evolves into a steady state within a few seconds. An example of a deformed interface computed in this way is shown in figure 4(b). A liquid film of thickness 5 mm was used for illustrative purposes (although we note that the thin-film equation is not expected to be valid for such a thickness). Next, we use this deformed interface as the lower boundary for the gas domain and again assume that it is a solid wall and recompute the solution of the decoupled gas problem. It can be seen in figure 4(b) that the computed solution is qualitatively similar to the one in figure 4(a). We extract the gas stresses from this solutions and use these updated stresses to solve the thin-film equation again to obtain an updated steady-state interface shape. This procedure is repeated until a converged steady-state interface shape is achieved. Typically, we find that 2–3 iterations are sufficient.

Next, we will analyse in detail how the normal and tangential stresses exerted by the gas onto the interface behave when the gas flow rate varies for the case when the interface is modelled as a flat solid wall. The results are presented in figure 5. Panels (a) and (d) show the normal and tangential stresses for the gas flow rate q_g changing from 0.2 (red lines) to 1.8 slpm (blue lines) with the increment of 0.2 slpm. As expected, the stresses grow as the gas flow rate increases. The normal stresses have their maximum values in the centre (at $R = 0$) and then rapidly decay as the radial distance increases. The tangential stresses vanish at the centre and have their maximum values at a distance slightly away from the centre, at approximately $R = 0.1$ cm. Then they slowly decay as R increases up to approximately $R = 1.2$ cm. After this distance, the tangential stresses become negligibly small, and this may be associated with the presence of a slow recirculation zone in the corner, as seen in figure 4. Panels (b) and (e) show the maxima of the normal and tangential stresses (blue lines), respectively, versus the gas flow rate, q_g , on the log-log scale and suggest a power law behaviour, i.e. $\max N_s$ scales approximately as q_g^2 and $\max T_s$ scales approximately as $q_g^{1.45}$. Indeed, the red dashed lines in panels (b) and (e) have slopes 2 and 1.45, respectively. It can be observed that the scaling for the normal stresses works well for all the values of the flow rate, whereas for the tangential stresses the scaling works better for larger values of the flow rate. We plotted the rescaled normal and tangential stresses N_s/q_g^2 and $T_s/q_g^{1.45}$ in panels (c) and (f), respectively. For the normal stresses, we can observe that the curves seem to collapse onto the same universal curve (except for the smallest gas flow rate for which there is a slight deviation, see the red curve). For the tangential stresses, the scaling works very well only for a relatively small range of R values. After the maxima at approximately $R = 0.1$ cm, the curves start to deviate from each other, but seem to approach a universal curve for larger values of q_g . The scaling for the normal stress follows from the fact that the stagnation point pressure (i.e. the pressure or normal stress where the gas jet impinges on the wall at $R = 0$) is associated with the dynamic pressure at the centre line of the gas jet, which follows from Bernoulli's theorem (assuming incompressible flow), see e.g. Cheslak *et al.* (1969); Clancy (2006). The scaling then follows from the fact that the dynamic pressure is proportional to the square of the jet velocity, which in turn is proportional to the flow rate q_g . The reason for the apparent scaling for the tangential stresses is not immediately obvious from the governing equations and is left as a topic for future investigation. We can conclude that these scalings may be utilised for larger values of the gas flow rate (particularly for thin films where the interface is not deformed much), but for smaller gas flow rates these scalings do not work well and the stresses need to be recomputed for each value of q_g (this particularly applies to tangential stresses).

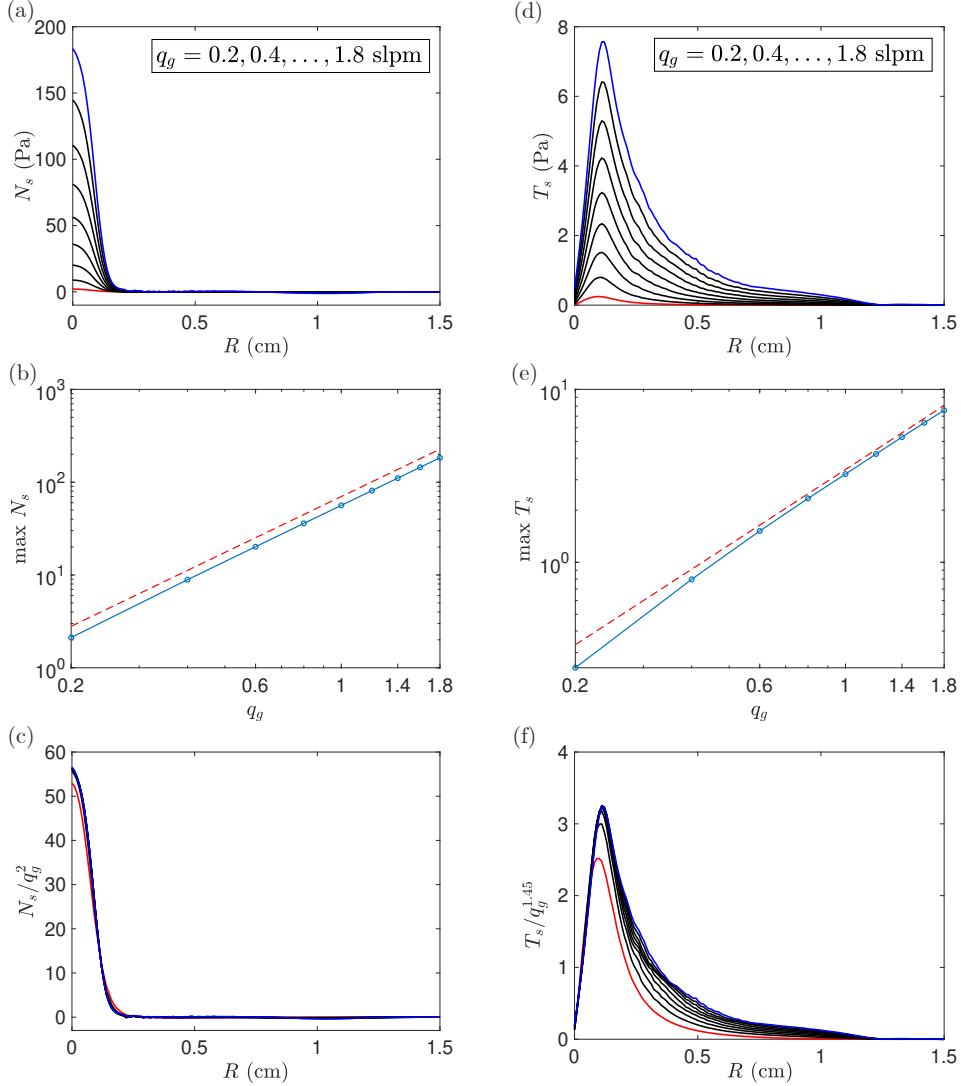


FIGURE 5. Stresses exerted by the gas onto the gas-liquid interface modelled as a flat solid wall. Panels (a)–(c) correspond to normal stresses and (d)–(f) correspond to tangential stresses. (a) and (d) show the stresses for the gas flow rate q_g changing from 0.2 to 1.8 slpm (red and blue lines, respectively) with the increment of 0.2 slpm. (b) and (e) show the maxima of the stresses (blue lines) versus q_g on the log-log scale. The red dashed lines have slopes 2 and 1.45 for the normal and tangential stresses, respectively. (c) and (f) show the rescaled stresses N_s/q_g^2 and $T_s/q_g^{1.45}$, respectively.

4.2. Comparison of the thin-film model with DNS and experiments

In this section, we present results for a film of thickness 0.5 mm. We start with the gas flow rate of 0.2 slpm at which the film deforms but does not rupture. The results are given in figure 6. Panels (a) and (b) show the normal and tangential stresses, respectively, exerted on the interface. These are computed using the iterative procedure described above. The blue solid lines correspond to the flat interface, the black dotted lines correspond to the curved interface, obtained by solving the thin-film equation (2.51), after the first iteration, and the red dashed lines are obtained for the curved interface after the second iteration.

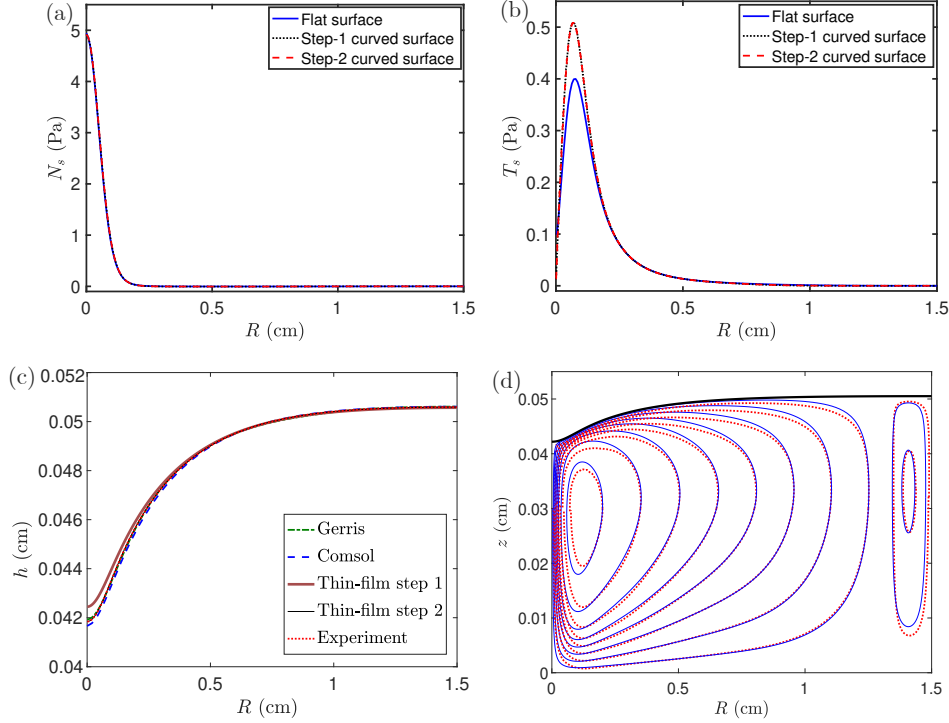


FIGURE 6. Numerical results for a gas jet of flow rate $q_g = 0.2$ slpm impinging onto a liquid film of thickness $h_0 = 0.5$ mm. Panels (a) and (b) show the normal and tangential stresses exerted by the gas on the interface and computed using the iterative procedure discussed in § 4.1. The first three iterations are shown: for a flat interface and for two subsequent deformed interfaces, as indicated in the legends. Panel (c) shows the resulting interface deformations at steady state obtained using *Gerris* and COMSOL for the fully coupled gas–liquid model, as well as the thin-film equation (2.51) with the iterative procedure, as indicated in the legend. An experimental result is also shown. Panel (d) shows the streamlines in the liquid film obtained using the thin-film equation and COMSOL (the blue solid and red dotted lines, respectively).

It can be observed that two iterations are sufficient in this case and convergence is achieved. There is only a minor difference in the results for the normal stresses. However, there is a noticeable difference between the tangential stresses computed for flat and curved interfaces. The resulting interface deformations for this gas flow rate are shown in panel (c) after the computational time $t = 5$ s, although to converge to a steady state approximately 2–3 seconds was found to be sufficient. In panel (c), we compare the thin-film results computed with the gas stresses obtained using the different stages of the iterative procedure (the brown thick solid and black thin solid lines) with the *Gerris* and COMSOL results for the fully coupled gas–liquid model (the green dash-dotted and blue dashed lines, respectively). An experimental result is also shown (the red dotted line). There is a slight difference in the region near $R = 0$ between the *Gerris* and COMSOL results for the fully coupled model and the thin-film result when the gas stress were computed by assuming that the interface was flat. This difference is nearly eliminated after the iterative procedure, and we conclude that the thin-film equation performs well even for a film thickness well beyond the expected range of validity of the equation. Panel (d) shows the streamlines in the liquid film obtained using the thin-film model (blue solid lines) and COMSOL (red dotted lines). We can observe that there is a relatively large eddy close to the axis of symmetry at $R = 0$ and there is a smaller and slower eddy near

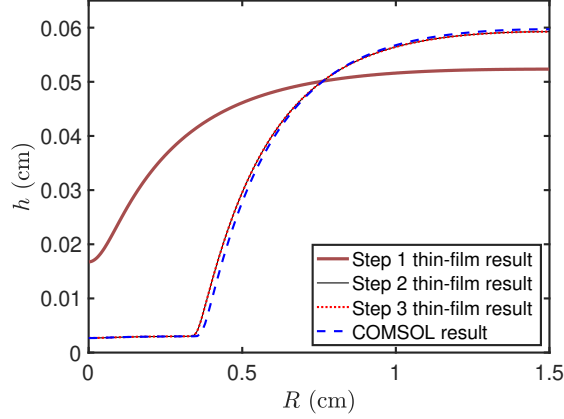


FIGURE 7. Numerical results for a gas jet of flow rate $q_g = 0.37$ slpm impinging onto a liquid film of thickness $h_0 = 0.5$ mm. Shown are the resulting interface deformations at steady state obtained using the thin-film equation (2.51) with the iterative procedure and COMSOL for the fully coupled gas-liquid model, as indicated in the legend. The numerical formulations include the disjoining pressure (2.13) giving the equilibrium contact angle $\theta_{eq} = 15^\circ$ and the precursor thickness $h_{eq} = 0.03$ mm.

the side wall of the beaker. This second eddy appears due to small and slow eddy in the gas in the corner between the gas-liquid interface and the side wall, see figure 4. We note that the *Gerris* results for the streamlines are in qualitative agreement with this.

The importance of the iterative procedure in computing gas stresses becomes more apparent when the gas flow rate is close to the value that leads to dewetting of the liquid from the bottom of the beaker. An example is shown in figure 7 for gas flow rate $q_g = 0.37$ slpm. To account for possible dewetting, the thin-film and COMSOL numerical simulations here include the disjoining pressure (2.13) with $A = 2.9609 \times 10^{-11}$ and $B = 8.2659 \times 10^{-25}$ giving the contact angle $\theta_{eq} = 15^\circ$ and the precursor thickness $h_{eq} = 0.03$ mm. It can be seen that in the COMSOL simulation for the fully coupled gas-liquid model a dry spot for radius of approximately 0.36 cm appears in the centre (blue dashed line). However, for the first step of the iterative procedure for the thin-film model we find that no dry spot appears. This is then suitably accounted for by the next step of the iterative procedure. Indeed, when we recompute the stresses for the resulting deformed interface and use them in the thin-film equation again, we observe that dewetting is initiated and a dry spot appears of radius that is in good agreement with the COMSOL result (see the black thin line). The next iteration on the gas stresses and the thin-film equation leads to the result that is indistinguishable from the one in the previous iteration.

4.3. Dewetting

Before discussing dewetting induced by gas jets, it is useful to analyse the linear stability of flat-film equilibrium solutions in the absence of the gas jet as well as to construct bifurcation diagrams of various non-equilibrium solutions. It will be shown later that many of the observed behaviours in gas-jet-induced dewetting can be explained by such an analysis.

4.3.1. Linear stability analysis and equilibrium solutions

We will utilise the thin-film equation (2.51) for our analysis. We consider a liquid film in the absence of a gas jet and analyse steady-state solutions of the thin-film equation, which takes the form

$$h_t + \frac{1}{R} \left[\frac{Rh^3}{3} \left(\frac{1}{R} (Rh_R)_R - Bo h + \bar{\Pi}(h) \right) \right]_R = 0. \quad (4.1)$$

Due to the destabilising effect of the long-range attractive forces, a sufficiently thin film must become linearly unstable. In (4.1) distances have been non-dimensionalised with the undisturbed film thickness, h_0 , making the undisturbed dimensionless film thickness is 1, so varying the dimensional film thickness is equivalent to varying the dimensionless parameters (and the dimensionless domain size). Thus, we consider the dimensionless equation (4.1) and perform the linear stability analysis of the solution $h \equiv 1$ to find out the linear instability conditions in terms of the dimensionless parameters. Note that the linear stability analysis for a similar equation but with the disjoining pressure containing only a destabilising term was performed by Witelski & Bernoff (2000). Substituting $h(R, t) = 1 + h_1(R, t)$ into (4.1) and assuming that $|h_1(R, t)| \ll 1$, we obtain the following linearised equation:

$$h_{1t} = \mathcal{L}[h_1] \equiv -\frac{1}{R} \left[\frac{R}{3} \left(\frac{1}{R} (Rh_{1R})_R + (\bar{\Pi}'(1) - Bo) h_1 \right) \right]_R. \quad (4.2)$$

The associated boundary conditions are

$$h_{1R} = 0, \quad h_{1RRR} = 0 \quad \text{at} \quad R = 0 \quad (4.3)$$

and

$$h_{1R} = 0, \quad Rh_{1RRR} + h_{1RR} = 0 \quad \text{at} \quad R = \bar{R}_b. \quad (4.4)$$

It can be concluded from Witelski & Bernoff (2000) that the eigenvalues of the operator \mathcal{L} are given by

$$\lambda_n = \frac{1}{3} [-\Lambda_n^4 + (\bar{\Pi}'(1) - Bo) \Lambda_n^2], \quad n = 1, 2, \dots, \quad (4.5)$$

where Λ_n 's are the eigenvalues of the Helmholtz problem

$$\frac{1}{R} (Rh_{1R})_R + \Lambda^2 h_1 = 0, \quad (4.6)$$

with $h_R = 0$ at $R = 0$ and at $R = \bar{R}_b$. The eigenfunctions of \mathcal{L} are the corresponding eigenfunctions of the Helmholtz problem. The eigenvalues of the Helmholtz problem are real, and it is enough to consider the positive ones. Assuming that the smallest positive eigenvalue is Λ_1 , the condition for linear instability becomes $\lambda_1 > 0$, or, equivalently,

$$Bo < \bar{\Pi}'(1) - \Lambda_1^2. \quad (4.7)$$

The eigenvalues of the Helmholtz problem are solutions of the equation $J_1(\Lambda \bar{R}_b) = 0$, where J_1 is the first-order Bessel function of the first kind. Denoting the smallest positive root of J_1 by $x_1 \approx 3.832$, we then find that $\Lambda_1 = x_1 / \bar{R}_b$. The corresponding eigenfunction is $J_0(\Lambda_1 R)$, where J_0 is the zeroth-order Bessel function of the first kind. The linear instability condition becomes

$$Bo < \bar{\Pi}'(1) - \frac{x_1^2}{\bar{R}_b^2}. \quad (4.8)$$

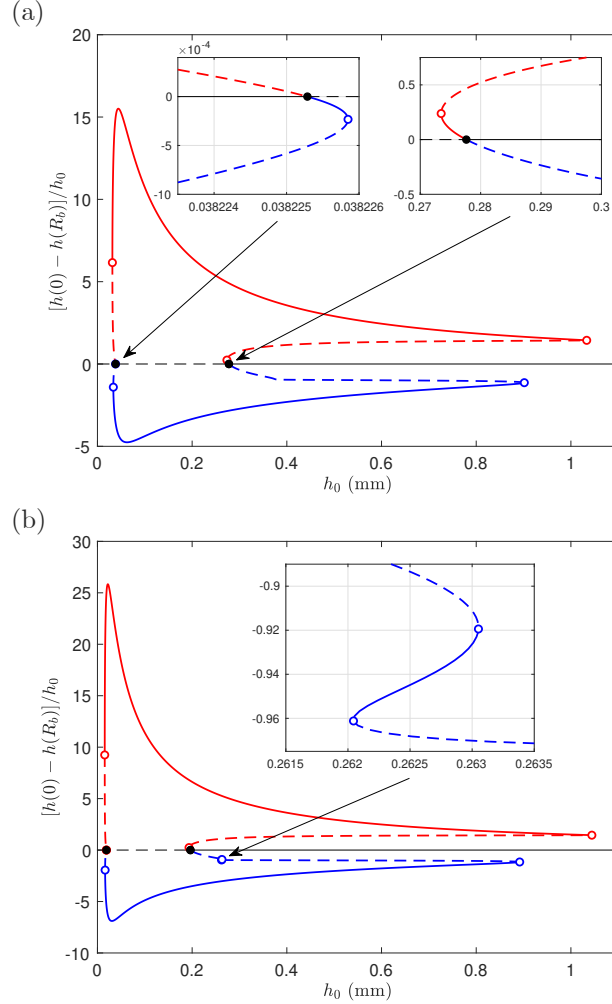


FIGURE 8. Bifurcation diagrams of steady-state solutions of the thin-film equation (4.1) when the equilibrium contact angle is $\theta_{eq} = 30^\circ$ and the precursor thickness is (a) $h_{eq} = 0.03$ mm or (b) $h_{eq} = 0.015$ mm showing the dependence of the dimensionless quantity $[h(0) - h(R_b)]/h_0$ on the undisturbed film thickness h_0 . The branches of flat solutions are shown in black. The branches of solutions with a minimum at $R = 0$ are below the horizontal line at zero (and are shown in blue). The branches of solutions with a maximum at $R = 0$ are above the horizontal line at zero (and are shown in red). The parts of the branches corresponding to stable and unstable solutions are shown with solid and dashed lines, respectively. The primary bifurcation points on the branches of flat-film solutions are indicated with black filled circles. Empty circles correspond to turning points on the branches.

In terms of the dimensional parameters, this condition can be rewritten as

$$\left(\frac{\rho_l g}{\gamma} + \frac{x_1^2}{R_b^2}\right)h_0^7 - \frac{3A}{\gamma}h_0^3 + \frac{6B}{\gamma} < 0. \quad (4.9)$$

For a given equilibrium precursor thickness, it can be verified that the inequality (4.9) has solutions if the contact angle is sufficiently large. For example, taking $h_{eq} = 0.03$ mm, we find that the liquid film may become linearly unstable if $\theta \gtrsim 1.21^\circ$, and taking $h_{eq} = 0.015$ mm, we find that the liquid film may become linearly unstable if $\theta \gtrsim 0.61^\circ$.

If the latter condition is satisfied, we find that there exist a range of film thicknesses, $h_0 \in (h_a, h_b)$, for which the flat film solution is linearly unstable. For example, for $h_{eq} = 0.03$ mm and $\theta_{eq} = 30^\circ$, we find that $h_a \approx 0.03822516$ mm and $h_b \approx 0.27959481$ mm, and for $h_{eq} = 0.015$ mm and $\theta_{eq} = 30^\circ$, we find that $h_a \approx 0.01911091$ mm and $h_b \approx 0.19778522$ mm. (Overall, h_a and h_b become smaller as h_{eq} decreases for a given value of θ_{eq} .) According to the bifurcation theory, for film thicknesses close to the values h_a and h_b at which linear stability of the uniform-thickness solution changes, there exist non-uniform solutions that bifurcate from the uniform solutions. (There of course exist other branches of solutions that bifurcate from the points where more modes become unstable. Such solutions are, however, less relevant to the present study and we do not discuss them here.) The nature of the bifurcations can be analysed by utilising a weakly nonlinear analysis to obtain the evolution equation for the amplitude of the unstable mode $J_0(\Lambda_1 R)$, see e.g. Witelski & Bernoff (2000) for a similar analysis. It turns out that the bifurcations are transcritical, and this is demonstrated e.g. in figure 8(a) for $h_{eq} = 0.03$ mm and $\theta_{eq} = 30^\circ$, which shows the bifurcation diagram of the non-uniform solutions when h_0 is used as the bifurcation parameter. We use the dimensionless quantity $[h(0) - h(R_b)]/h_0$ as a measure of the interfacial shape distortion of the solutions. The uniform solutions then correspond to the horizontal line with the measure equal to zero (see the black line). The solid lines show stable solutions and the dashed lines show unstable solutions. The black filled circles show the primary bifurcation points. We find that these points are connected with each other by branches of non-uniform solutions, and, in fact, we find that from each of the primary bifurcation points there emerge two types of solutions. Namely, we obtain solution which have a maximum at $R = 0$ (the corresponding branch is above the horizontal line at zero and is shown in red). For $h_0 = h_a$, we find that this branch initially goes to the left and is initially unstable up to the first turning point (the turning points are shown with empty circles). For $h_0 = h_b$, we find that this branch also initially goes to the left and is initially stable. We also obtain solution which have a minimum at $R = 0$ (the corresponding branch is below the horizontal line at zero and is shown with blue colour). Solutions of this type are more relevant to the study of the deformation of liquid films under gas jets, and we will, therefore, discuss them in more detail. For $h_0 = h_a$, we find that this branch initially goes to the right and is initially stable for a very small range of values of h_0 (up to the turning point at $h_0 = h_{t1} \approx 0.03822585$ mm). After the turning point at $h_0 = h_{t1}$ the branch becomes unstable up to the second turning point at $h_0 = h_{t2} \approx 0.03355743$ mm. Then, the solutions become stable up to the next turning point at $h_0 = h_{t3} \approx 0.9016$ mm. The next part of the bifurcation curve is unstable and goes to the left terminating at the primary bifurcation point, $h_0 = h_b$. The insets in the figure zoom into the regions around the primary bifurcation points and confirm the transcritical nature of the bifurcations.

We conclude that for $h_0 > h_{t3}$ stable non-uniform solutions having a minimum in the centre do not exist. Thus, if we consider a film of an average thickness $h_0 > h_{t3}$ that was initially deformed by a gas jet with the gas flow switched off after some time, we expect the dry spot to heal with time with the liquid film eventually levelling up and returning to a uniform-thickness state. Note that the healing process of liquid films has been analysed in detail by Dijksman *et al.* (2015), Bostwick *et al.* (2017), Zheng *et al.* (2018), and in Zheng *et al.* (2018) in particular it has been shown that there exists self-similarity in the healing process and the solutions that govern the healing process are self-similar solutions of the second kind.

For $h_0 \in (h_b, h_{t3})$, in addition to stable uniform-thickness solutions, there exist stable nonuniform-thickness solutions which have a form of dewetted liquid films with a dry spot in the centre. (As mentioned above, we ignore solutions with a maximum at $R = 0$ as these

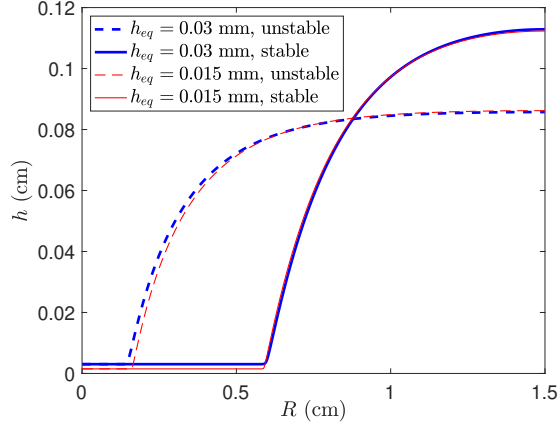


FIGURE 9. Steady-state solutions with a minimum at $R = 0$ of the thin-film equation (4.1) when the average film thickness is $h_0 = 0.8$ mm, the equilibrium contact angle is $\theta_{eq} = 30^\circ$ and the precursor thickness is $h_{eq} = 0.03$ mm (thick blue lines) or $h_{eq} = 0.015$ mm (thin magenta lines). The solid and dashed lines correspond to stable and unstable solutions, respectively.

are not relevant to our study.) These solutions are separated from the uniform-thickness solutions by an unstable part of the branch of nonuniform solutions. The solutions of this unstable part of the branch also have a form of dewetted liquid films with a dry spot in the centre for $h_0 \gtrsim 0.38$ mm but with the smaller radii of the dry spots compared to the dry spots for the corresponding stable solutions. For $h_0 \lesssim 0.38$ mm the solutions of the unstable part have a localised minimum in the centre, with the thickness greater than the precursor film thickness, so that a dry spot does not appear. The stable and unstable solutions for $h_0 = 0.8$ mm are shown in figure 9 with the thick (blue) solid and dashed lines, respectively. As regards a liquid film deformed by a gas jet for such film thicknesses, we expect that if the gas flow rate is not strong enough, the liquid film may initially dewet in the centre but then return to the uniform state after the gas jet is switched off. However, if the gas jet is strong enough to push the liquid film profile beyond the unstable non-uniform solution, we expect that the liquid film remains dewetted in the centre even after the gas flow is switched off.

For $h_0 \in (h_{t1}, h_b)$, the uniform thickness solution is linearly unstable and we therefore expect that for any gas flow rate the liquid film will dewet and remain dewetted even after the gas flow is switched off. We are not interested in the behaviour of very thin liquid films of thicknesses close to or smaller than the precursor-film thickness and thus we do not discuss the expected behaviour for $h_0 < h_{t1}$.

In figure 8(b), we show the bifurcation diagram of the non-uniform solutions for the same equilibrium contact angle ($\theta_{eq} = 30^\circ$) as in figure 8(a) but for a twice as thin equilibrium precursor thickness, $h_{eq} = 0.015$ mm. We notice that the bifurcation diagram agrees well with the one for $h_{eq} = 0.03$ mm, particularly for larger values of h_0 . One qualitative difference is the appearance of two additional turning points on the branch of non-uniform solutions with the minimum in the centre, at $h_0 = h_{t4} \approx 0.262$ and at $h_0 = h_{t5} \approx 0.263$. This can be clearly seen in the inset zooming into the region around these turning points. This implies that there is a small range of the film thicknesses, $h_0 \in (h_{t4}, h_{t5})$, where there exist additional stable non-uniform-thickness solutions that have a localised minimum in the centre (without a dry spot). To confirm qualitative and quantitative similarity of the results for $h_{eq} = 0.015$ mm with the results for $h_{eq} = 0.03$ mm for larger values of h_0 , we show in figure 9 the stable and unstable solutions

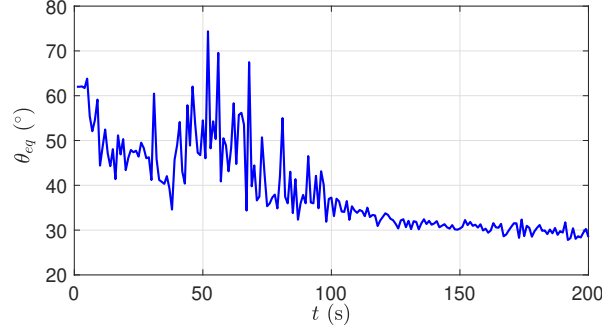


FIGURE 10. An experimental result for the evolution of the contact angle that a drop of water makes with the acrylic polymer used in experiments for gas-jet induced dewetting measured using the Drop Shape Analyser DSA100 by KRÜSS.

for $h_0 = 0.8\text{ mm}$ when $h_{eq} = 0.015\text{ mm}$ with the thin (red) solid and dashed lines, respectively, in addition to the corresponding solutions for $h_{eq} = 0.03\text{ mm}$. We indeed observe that the results for $h_{eq} = 0.03\text{ mm}$ and $h_{eq} = 0.015\text{ mm}$ agree very well.

4.3.2. Dewetting induced by gas jets

We first consider a liquid film of thickness $h_0 = 0.2\text{ mm}$. For such a thin film, we used $h_{eq} = 0.01\text{ mm}$ for the COMSOL and thin-film computations. To compare with experiments, we measured the equilibrium contact angle for the bottom of the beaker made of an acrylic polymer. This was done by placing a drop of water onto a plate made of the acrylic polymer and measuring the resulting angle using the Drop Shape Analyser DSA100 by KRÜSS. The experimental results showing the evolution of the contact angle θ_{eq} over time are given in figure 10 and indicate that $\theta_{eq} \approx 30^\circ (\pm 2^\circ)$. Using the analysis from the previous section, it can be shown that for such values of θ_{eq} and h_{eq} , a water film of thickness $h_0 = 0.2\text{ mm}$ is linearly stable, but this value is close the value $h_b \approx 0.1615\text{ mm}$ below which the liquid film becomes linearly unstable. This indicates that a gas jet of a relatively weak flow rate can destabilise the liquid film so that it would dewet leaving a dry spot in the centre of the beaker. This is confirmed by our numerical simulations using all the three different approaches (*Gerris*, COMSOL and the thin-film model). Figure 11(a) shows dewetted liquid film profiles after $t = 1\text{ s}$ for the gas flow rates $q_g = 0.2, 0.4$ and 0.8 slpm using DNS in COMSOL. It can be observed that the profiles converge to the same steady state independent of the gas flow rate. We note that the simulations with the thin-film model produce the profiles which are in excellent agreement with the COMSOL results. The *Gerris* simulations also agree very well with these results (with a very small difference in the amplitude for the final film profile due to the fact that for the *Gerris* simulations there is no precursor film and thus the volume of the liquid in the final wetted region is slightly bigger). We, therefore, do not show the thin-film and *Gerris* results in figure 11(a) (detailed comparisons are discussed below for thicker water films). An experimental result for a dewetted water film of thickness 0.2 mm induced by a gas jet of flow rate 0.4 slpm is given in figure 11(b) which shows a top view for the final profile. The radius of the dry spot turns out to be $R_d \approx 1.13\text{ mm}$, which agrees well with the numerical simulations in which the radius is approximately $R_d \approx 1.12\text{ mm}$ in the *Gerris* calculation and 1.17 mm in COMSOL. In this case, we can conclude that the gas jet is important for initialising dewetting, but dewetting itself is dominated by the receding contact line motion until the equilibrium contact angle is reached. The gas jet does not affect the final steady-state profile. This can be explained by the fact that

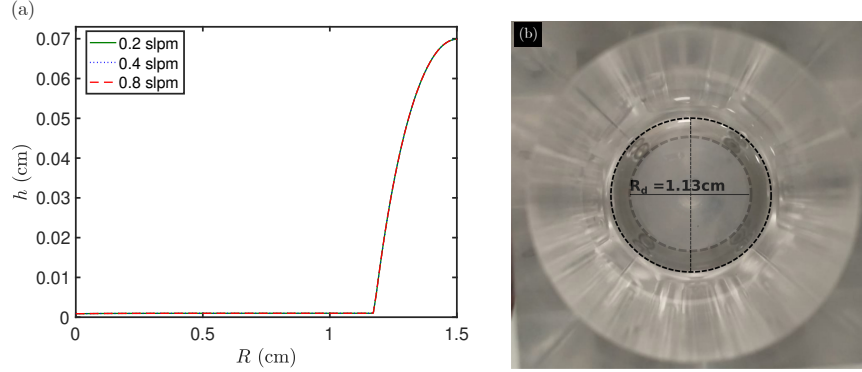


FIGURE 11. (a) COMSOL numerical solutions for dewetting of a water film of initial thickness 0.2 mm induced by the gas jets of flow rates $q_g = 0.2, 0.4$ and 0.8 slpm (green solid, blue dotted and red dashed lines, respectively) obtained using $\theta_{eq} = 30^\circ$ and $h_{eq} = 0.01$ mm. The profiles correspond to time $t = 1$ s, at which steady states are reached. (b) A top view for the final profile for an experiment of dewetting of a water film of thickness 0.2 mm induced by a gas jet of flow rate 0.4 slpm.

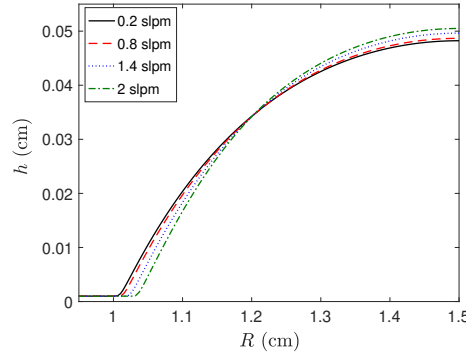


FIGURE 12. (a) COMSOL numerical solutions for dewetting of a water film of initial thickness 0.2 mm induced by the gas jets of flow rates $q_g = 0.2, 0.8, 1.4$ and 2 slpm, as indicated in the legend, obtained using $\theta_{eq} = 15^\circ$ and $h_{eq} = 0.01$ mm. The profiles correspond to time $t = 1$ s, at which steady states are reached.

for the equilibrium solution the wetted region is such that the gas normal and tangential stresses are negligibly small, see figures 5(a,d). Numerical results obtained in COMSOL for the final steady-state profiles for the case of a smaller contact angle and the same film thickness are shown in figure 12 for the gas flow rates $q_g = 0.2, 0.8, 1.4$ and 2 slpm. In this case, the radius of the dry spot for the steady-state solutions is approximately 1 mm, and the influence of the gas jet, although weak, becomes noticeable. As expected, the stronger the gas flow the larger the radius of the dry spot becomes. By looking at the gas normal and tangential stresses in figures 5(a,d), we can notice again that normal stresses are negligible in the wetted area, but now there are small but non-negligible tangential stresses when $R \approx 1$ mm, which push the liquid away from the centre.

Now we consider a thicker water film with $h_0 = 0.5$ mm and we assume that $\theta_{eq} = 30^\circ$ and $h_{eq} = 0.03$ mm. Figure 13(a) shows liquid film profiles after $t = 1$ s for the gas flow rates $q_g = 0.2, 0.3, 0.4$ and 0.5 slpm (see the black, green, red and blue lines, respectively). Note that at $t = 1$ s steady state profiles are reached. This can be confirmed in figures 13(b,c) showing the evolutions of the minimum and maximum values of the

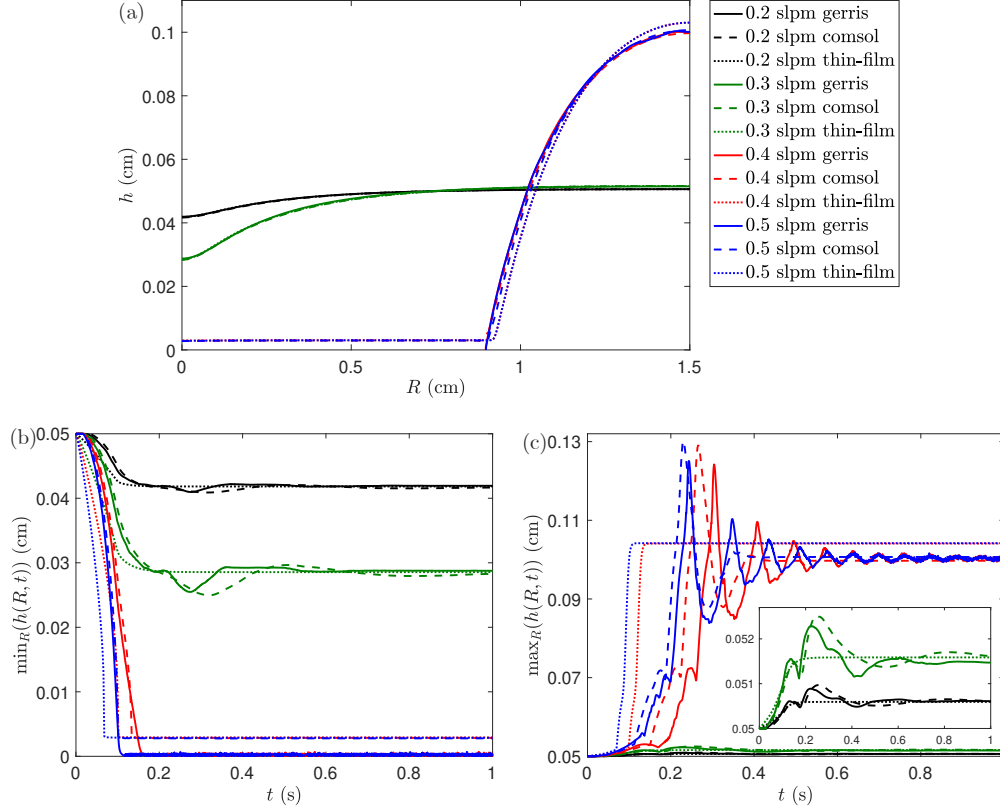


FIGURE 13. Numerical solutions for the evolution of a water film of thickness 0.5 mm under the gas jets of flow rates $q_g = 0.2, 0.3, 0.4$ and 0.5 slpm (black, green, red and blue lines, respectively) obtained using $\theta_{eq} = 30^\circ$ and $h_{eq} = 0.03$ mm. The results obtained using *Gerris*, COMSOL and the thin-film equation are shown with the solid, dashed and dotted lines, respectively. Panel (a) shows the profiles at time $t = 1$ s. Panels (b) and (c) show the evolutions of the minimum and maximum values of the profiles, respectively.

profiles, respectively. We show the results obtained using *Gerris*, COMSOL and the thin-film equation, see the solid, dashed and dotted lines, respectively. All the models agree very well, particularly as far as the final profiles are concerned. The evolutions of the minimum and maximum values obtained using *Gerris* and COMSOL show qualitative agreement and indicate oscillatory approach toward steady states indicating the presence of interfacial oscillations/waves. The results obtained using the thin-film equation also show reasonably good agreement with the *Gerris* and COMSOL results, but do not feature oscillations. This may be due to the fact that for such a thickness of the film inertial effects become important and cannot be neglected to accurately describe the evolution of the liquid film. We can observe that dewetting is initiated for a gas flow rate between 0.3 and 0.4 slpm, and, as before, the final dewetted profiles do not depend much on the strength of the gas jet. This also agrees with our experimental observations.

Next, we consider even thicker water films with $h_0 = 0.8$ mm and $h_0 = 1$ mm, see figures 14 and 15, respectively. As before, we assume that $\theta_{eq} = 30^\circ$ and $h_{eq} = 0.03$ mm. Panels (a) and (b) show the evolutions of the minimum and maximum values of the profiles, respectively. For $h_0 = 0.8$ mm we used the gas flow rates $q_g = 0.5, 0.525, 0.6$ and 0.5 slpm (see the black, green, red and blue lines, respectively, in figure 14) and we switched off the gas flow at $t = 0.25$ s. The solid parts of the curves correspond to the

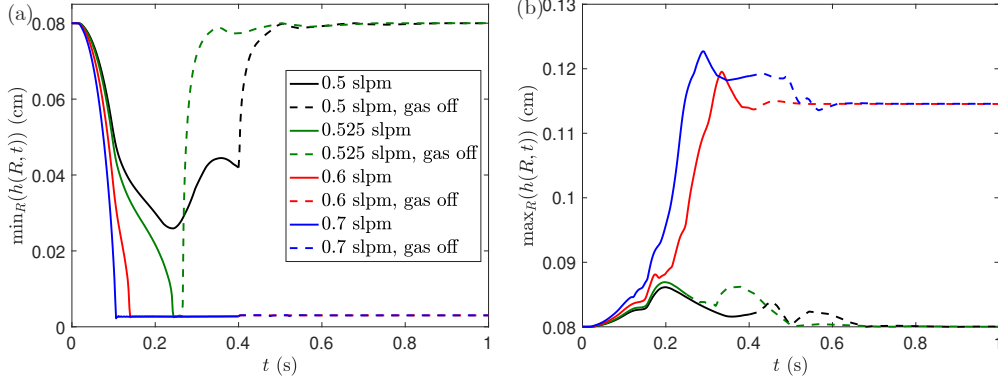


FIGURE 14. COMSOL numerical solutions for the evolution of a water film of thickness 0.8 mm under the gas jets of flow rates $q_g = 0.5, 0.525, 0.6$ and 0.7 slpm (black, green, red and blue lines, respectively) obtained using $\theta_{eq} = 30^\circ$ and $h_{eq} = 0.03$ mm. Panels (a) and (b) show the evolutions of the minimum and maximum values of the profiles, respectively. The gas flow was switched off at $t = 0.25$ s.

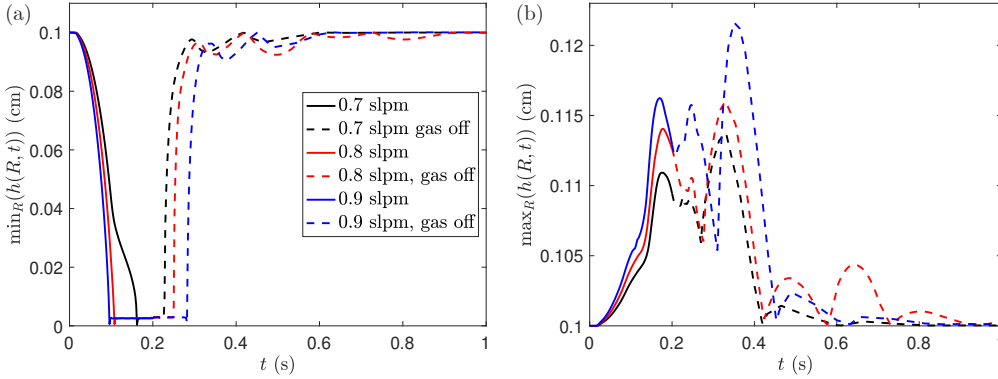


FIGURE 15. COMSOL numerical solutions for the evolution of a water film of thickness 1 mm under the gas jets of flow rates $q_g = 0.7, 0.8$ and 0.9 slpm (black, red and blue lines, respectively) obtained using $\theta_{eq} = 30^\circ$ and $h_{eq} = 0.03$ mm. Panels (a) and (b) show the evolutions of the minimum and maximum values of the profiles, respectively. The gas flow was switched off at $t = 0.2$ s.

gas flow switched on and the dashed parts correspond to the gas flow switched off. We can observe that dewetting is initiated for a gas flow rate between 0.5 and 0.525 slpm. However, for $q_g = 0.525$ slpm we find out that after the gas flow is switched off, the dry spot in the centre heals and the liquid films returns to the uniform thickness state. This agrees with the theoretical analysis of § 4.3.1, where we predicted (using the thin-film equation) the coexistence of stable uniform thickness and dewetted solutions in the absence of gas flow. We also predicted that for a relatively weak gas flow the liquid film may dewet in the centre but then heal and return to the uniform thickness state after the gas flow is switched off, as we indeed observe for $q_g = 0.525$ slpm. For $q_g = 0.6$ and $q_g = 0.7$ slpm, we observe that the liquid film remains dewetted even after the gas flow is switched off, in agreement with the theoretical prediction of § 4.3.1. This is also confirmed using *Gerris* simulations.

For $h_0 = 1$ mm, the theoretical prediction was that the liquid film should heal after switching off the gas flow, no matter how strong the gas flow was. This is confirmed in figures 15, where we used the gas flow rates $q_g = 0.7, 0.8$ and 0.9 slpm (see the black, red,

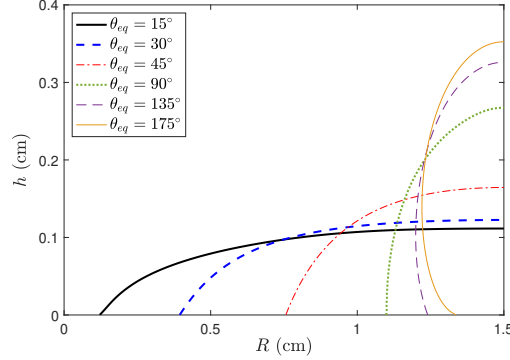


FIGURE 16. *Gerris* numerical solutions for dewetting of a water film of thickness 1 mm induced by the gas jet of flow rate $q_g = 1$ slpm for $\theta_{eq} = 15^\circ, 30^\circ, 45^\circ, 60^\circ, 90^\circ, 135^\circ$ and 175° as indicated in the legend. The profiles correspond to time $t = 3$ s, at which steady states are reached.

and green lines, respectively). We switched off the gas flow at $t = 0.2$ s. The solid parts of the curves correspond to the gas flow switched on and the dashed parts correspond to the gas flow switched off. In all the cases, the liquid film returns to the uniform thickness state.

Finally, we analyse dewetting of a water film of thickness $h_0 = 1$ mm for the gas flow rate $q_g = 1$ slpm but for different equilibrium contact angles. We consider $\theta_{eq} = 15^\circ, 30^\circ, 45^\circ, 60^\circ, 90^\circ, 135^\circ$ and 175° in figure 16, illustrating interface profiles at time $t = 3$ s, at which steady states are reached. These results were obtained using *Gerris*, as for contact angles greater than 90° our COMSOL implementation and thin-film model are not suitable. Videos showing the evolution of the water film for $\theta_{eq} = 15^\circ$ and 135° are included in the supplementary material. It can be observed that the approach to a steady state is non-monotonic in both cases, described instead by an oscillatory behaviour. In figure 16, we can observe that for larger contact angles the radius of the dry spot is larger, as expected. For $\theta_{eq} = 15^\circ$, we have confirmed the dry spot in the centre heals after the gas flow is switched off (as for $\theta_{eq} = 30^\circ$ as we discussed above). However, for the larger equilibrium contact angles the liquid film remains dewetted when the gas flow is switched off.

5. Conclusions

We have examined both experimentally and theoretically the flow arising from a gas jet (air) impinging axisymmetrically on a liquid (water) in a cylindrical beaker. The calculations were carried out using two models that involved DNS (COMSOL and *Gerris*) and a third based on a thin-film approximation. The deformation of the liquid surface, determined experimentally when a steady state had been reached, was shown to be in good agreement with the DNS results for all water depths, when the gas flow rate was low, and in the case of a thin liquid film with all three models. It was also shown that interface shapes and streamline patterns calculated using the thin film model were in agreement with DNS for film thicknesses much larger than those for which the thin-film approximation was strictly valid.

Experiments were used to determine interface shapes both in the steady state and during the development of a steady flow after the gas jet was switched on. The contact angle between the liquid and its container was also measured experimentally and this was used as an input into the theoretical models. In the thin-film case, when the gas

flow rate was high enough, dewetting of the film from the surface occurred. Using the experimentally measured contact angle of 30° and a precursor thickness of $h_{eq} = 0.1$ mm, a parameter determined from the disjoining pressure incorporating long-range and short-range intermolecular forces and used in the COMSOL formulation and the thin-film equation, the conditions for dewetting determined by all three models were found to be in good agreement with experiment.

Dewetting was also investigated using linear stability analysis of various steady-state solutions of the thin-film model for a range of values of initial film thicknesses, contact angles and values of h_{eq} . This analysis identified the various regimes in which dewetting could occur in agreement with the DNS and thin-film models. Regimes where the liquid would remain in its dewetted state or heal after the gas jet was turned off were identified.

For thicker films, the agreement between the models was less good for the time dependent flow before the final steady state was achieved, although the agreement for the steady states was still good. DNS results feature decaying interfacial oscillations/waves which were not present in the thin-film model, possibly due to the neglect of the inertial terms in the thin-film approximation. Experiments also showed the oscillations persisting for longer times than those predicted by the models (a video of an experiment for a 5 mm-thick water film and a gas jet of flow rate 1 slpm showing interfacial oscillations is included in the supplementary material). Indeed, preliminary experiments and DNS carried out over a range of gas flow rates for thicker films show that in some cases the oscillations do not decay at all, resulting in ‘self-sustained oscillations’ instead. The conditions for this to occur will be the subject of a future study.

Finally it should be pointed out that in the context of falling liquid films, accurate reduced-order models taking into account inertia have been developed using, for example, the weighted integral-boundary-layer approach (see e.g. Ruyer-Quil & Manneville 2000; Kalliadasis *et al.* 2011; Tseluiko & Kalliadasis 2011; Denner *et al.* 2016). Derivation and analysis of such models in the present context is left as a topic for future investigation.

We acknowledge the support of the UK Fluids Network (EPSRC Grant EP/N032861/1) in funding participation in a Special Interest Group meeting and a week-long Short Research Visit of RC to Loughborough University that shaped the direction of this work. CJO would like to acknowledge the Adventure Mini-CDT on Gas-Plasma Interactions with Organic Liquids at Loughborough University for the PhD studentship.

REFERENCES

- ABRÀMOFF, M., MAGALHÃES, P. & RAM, S. 2004 Image processing with ImageJ. *Biophotonics Int.* **111**, 36–42.
- ADIB, M., EHTEHAM, M. A. & TABRIZI, H. B. 2018 Numerical and experimental study of oscillatory behavior of liquid surface agitated by high-speed gas jet. *Appl. Math. Model.* **62**, 510–525.
- AFKHAM, S., BUONGIORNO, J., GUION, A., POPINET, S., SAADE, Y., SCARDOVELLI, R. & ZALESKI, S. 2018 Transition in a numerical model of contact line dynamics and forced dewetting. *J. Comput. Phys.* **374**, 1061–1093.
- BANKS, R. B. & CHANDRASEKHARA, D. V. 1963 Experimental investigation of the penetration of a high-velocity gas jet through a liquid surface. *J. Fluid Mech.* **15**, 13–34.
- BERENDSEN, C. W. J., ZEEGERS, J. C. H. & DARHUBER, A. A. 2013 Deformation and dewetting of thin liquid films induced by moving gas jets. *J. Colloid Interf. Sci.* **407**, 505–515.
- BERENDSEN, C. W. J., ZEEGERS, J. C. H., KRUIS, G. C. F. L., RIEPEN, M. & DARHUBER, A. A. 2012 Rupture of thin liquid films induced by impinging air-jets. *Langmuir* **28**, 9977–9985.

- BERGHMANS, J. 1972 Stability of a gas-liquid interface and its relation to weld pool stability. *J. Phys. D* **5**, 1096–1105.
- BOSTWICK, J. B., DIJKSMAN, J. A. & SHEARER, M. 2017 Wetting dynamics of a collapsing fluid hole. *Phys. Rev. Fluids* **2**, 014006.
- CHESLAK, F. R., NICHOLLS, J. A. & SICHEL, M. 1969 Cavities formed on liquid surfaces by impinging gaseous jets. *J. Fluid Mech.* **36**, 55–63.
- CLANCY, J. L. 2006 *Aerodynamics*. Sterling Book House.
- DENNER, F., PRADAS, M., CHAROGIANNIS, AL., MARKIDES, C. N., VAN WACHEM, B. G. M. & KALLIADASIS, S. 2016 Self-similarity of solitary waves on inertia-dominated falling liquid films. *Phys. Rev. E* **93**, 033121.
- DIJKSMAN, J. A., MUKHOPADHYAY, S., GAEBLER, C., WITELSKI, T. P. & BEHRINGER, R. P. 2015 Obtaining self-similar scalings in focusing flows. *Phys. Rev. E* **92**, 043016.
- FOSTER, J. E. 2017 Plasma-based water purification: Challenges and prospects for the future. *Phys. Plasmas* **24**, 055501.
- GALVAGNO, M., TSELUIKO, D., LOPEZ, H. & THIELE, U. 2014 Continuous and discontinuous dynamic unbinding transitions in drawn film flow. *Phys. Rev. Lett.* **112**, 137803.
- DE GENNES, P.-G., BROCHARD-WYART, F. & QUÉRÉ, D. 2013 *Capillarity and wetting phenomena: drops, bubbles, pearls, waves*. Springer New York.
- HE, A. & BELMONTE, A. 2010 Deformation of a liquid surface due to an impinging gas jet: A conformal mapping approach. *Phys. Fluids* **22**, 042103.
- HUGHES, A. P., THIELE, U. & ARCHER, A. J. 2015 Liquid drops on a surface: Using density functional theory to calculate the binding potential and drop profiles and comparing with results from mesoscopic modelling. *J. Chem. Phys.* **142**, 074702.
- HWANG, H. Y. & IRONS, G. A. 2012 A water model study of impinging gas jets on liquid surfaces. *Metall. Mater. Trans. B* **43**, 302–315.
- KALLIADASIS, S., RUYER-QUIL, C., SCHEID, B. & VELARDE, M. G. 2011 *Falling liquid films. Series on Applied Mathematical Sciences* 176. Springer, London.
- LACANETTE, D., GOSSET, A., VINCENT, S., BUCHLIN, J.-M. & ARQUIS, É. 2006 Macroscopic analysis of gas-jet wiping: numerical simulation and experimental approach. *Phys. Fluids* **18**, 042103.
- LIU, Q., CHEN, W., HU, L., XIE, H. & FU, X. 2015 Experimental investigation of cavity stability for a gas-jet penetrating into a liquid sheet. *Phys. Fluids* **27**, 082106.
- MOLLOY, N. A. 1970 Impinging jet flow in a two-phase system: the basic flow pattern. *J. Iron Steel Inst.* **208**, 943–950.
- MORDASOV, M. M., SAVENKOV, A. P. & CHECHETOV, K. E. 2016 Method for analyzing the gas jet impinging on a liquid surface. *Technical Physics* **61**, 659–668.
- MUÑOZ-ESPARZA, D., BUCHLIN, J. M., MYRILLAS, K. & BERGER, R. 2012 Numerical investigation of impinging gas jets onto deformable liquid layers. *Appl. Math. Model.* **36**, 2687–2700.
- NGUYEN, A. V. & EVANS, G. M. 2006 Computational fluid dynamics modelling of gas jets impinging onto liquid pools. *Appl. Math. Model.* **30**, 1472–1484.
- OLMSTEAD, W. E. & RAYNOR, S. 1964 Depression of an infinite liquid surface by an incompressible gas jet. *J. Fluid Mech.* **19**, 561–576.
- PISMEN, L. M. 2002 Mesoscopic hydrodynamics of contact line motion. *Colloids Surf. A* **206**, 11–30.
- POPINET, S. 2009 An accurate adaptive solver for surface-tension-driven interfacial flows. *J. Comput. Phys.* **228**, 5838–5866.
- PRYOR, R. W. 2011 *Multiphysics modeling using COMSOL®: a first principles approach*. Jones & Bartlett Learning.
- RAUSCHER, M. & DIETRICH, S. 2008 Wetting phenomena in nanofluidics. *Annu. Rev. Mater. Res.* **38**, 143–172.
- RUYER-QUIL, C. & MANNEVILLE, P. 2000 Improved modeling of flows down inclined planes. *Eur. Phys. J. B* **15**, 357–369.
- SIBLEY, D. N., SAVVA, N. & KALLIADASIS, S. 2012 Slip or not slip? a methodical examination of the interface formation model using two-dimensional droplet spreading on a horizontal planar substrate as a prototype system. *Physics of Fluids* **24**, 082105.
- SOLÓRZANO-LÓPEZ, J., ZENIT, R. & RAMÍREZ-ARGÁEZ, M. A. 2011 Mathematical and physical

- simulation of the interaction between a gas jet and a liquid free surface. *Appl. Math. Model.* **35**, 4991–5005.
- THORNTON, J. A. & GRAFF, H. F. 1976 An analytical description of the jet finishing process for hot-dip metallic coatings on strip. *Metall. Trans. B* **7**, 607–618.
- TIAN, W. & KUSHNER, M. J. 2014 Atmospheric pressure dielectric barrier discharges interacting with liquid covered tissue. *J. Phys. D* **47**, 165201.
- TSELUIKO, D. & KALLIADASIS, S. 2011 Nonlinear waves in counter-current gas–liquid film flow. *J. Fluid Mech.* **673**, 19–59.
- TUCK, E. O. 1975 On air flow over free surfaces of stationary water. *The ANZIAM Journal* **19**, 66–80.
- TURKDOGAN, E. T. 1966 Fluid dynamics of gas jets impinging on surface of liquids. *Chem. Eng. Sci.* **21**, 1133–1144.
- TURKDOGAN, E. T. 1996 *Fundamentals of Steelmaking*. Institute of Materials.
- VANDEN-BROECK, J. M. 1981 Deformation of a liquid surface by an impinging gas jet. *SIAM J. Appl. Math.* **41**, 306–309.
- VELLINGIRI, R., TSELUIKO, D. & KALLIADASIS, S. 2015 Absolute and convective instabilities in counter-current gas–liquid film flows. *J. Fluid Mech.* **763**, 166–201.
- VERLACKT, C. C. W., VAN BOXEM, W. & BOGAERTS, A. 2018 Transport and accumulation of plasma generated species in aqueous solution. *Phys. Chem. Chem. Phys.* **20**, 6845–6859.
- WITELSKI, T. P. & BERNOFF, A. J. 2000 Dynamics of three-dimensional thin film rupture. *Physica D* **147**, 155–176.
- ZHENG, Z., FONTELOS, M. A., SHIN, S., DALLASTON, M. C., TSELUIKO, D., KALLIADASIS, S. & STONE, H. A. 2018 Healing capillary films. *J. Fluid Mech.* **838**, 404–434.